Chapter 4

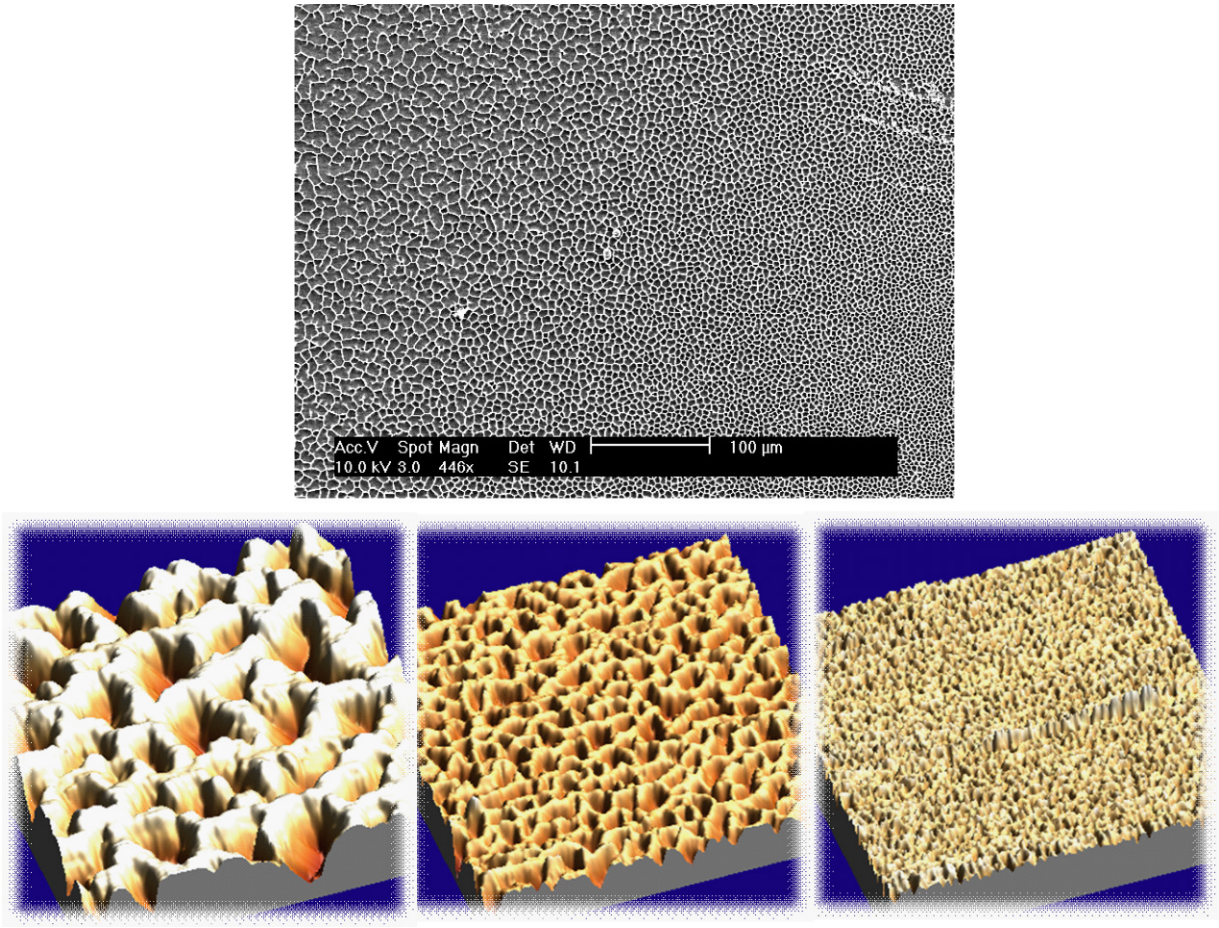

Asymmetric anodisation of silicon for biological and photonic applications

Chapter outline

In conventional pSi fabrication, one attempts to obtain a porous layer with uniform properties from the periphery to the center of the etched region. Asymmetry is therefore commonly avoided since that would give rise to non-uniform properties and dispersion effects. However, recent studies have shown an asymmetrical etching arrangement can lead to a pSi film with a lateral pore size gradient[1,2]. In this setup, the face of the electrode is held perpendicular relative to the surface of the silicon. This forces the current potential from electrode source within the electrolytic solution to vary as a function of distance from the counter electrode due to resistance of the electrolyte leading to a gradual decrease in current density as the distance from the electrode increases. If the current density applied is constant, the outcome during asymmetric anodisation will be a surface displaying a lateral gradient of pore sizes that can range from large (1 μm) to small (5 nm). The size range of these pores can be controlled by either modifying the anodic current or the HF concentration. Such pore size gradients can be useful for the evaluation of cellular behaviour[2] as well as specific protein adsorption[1].

Apart from producing differing pore sizes on the surface, the same anodising principle can be applied in tailoring of multilayered photonic pSi. If an alternating waveform is applied during the anodisation, a photonic profile with a spectrum of rejection bands can be produced on the film. Such photonic gradient can prove useful in applications such as gradient refractive index devices[3,4], MOEMS, photonic barcodes and also as biosensors[5]. In this chapter, we will explore some of the unique properties of these laterally graded pSi surfaces with regards to:

- **generating gradients of wettability,**
- **studying the behaviour of adherent mammalian cells and**
- **fabricating multidirectional photonic gradients.**

4.1 Control over wettability via surface modification of porous gradients

The solid-liquid interface is important in defining the degree of wettability (hydrophobicity/hydrophilicity) of a surface and subsequent interactions between the surface and components in the liquid contacting the surface. For example, the increasing demand for sophistication on biochip surfaces has motivated extensive studies of liquid-surface interaction[6,7]. It is important to note that biochip and material design usually involves tuning of wettability using surface chemistry[8-11] and in particular surface roughness[12,13] or a combination of texture and chemistry[14,15]. Surface wettability is a key factor in mediating fluid transport in confined spaces and across surfaces and it also influences adsorption of biomolecules and subsequent biological response. Therefore, control over wettability has significant applications in areas such as biomedical diagnostics and biomaterials.

In recent years, considerable attention had been directed towards self assembled monolayers (SAMs) and polymers with different wettability profiles to influence and modulate the levels of protein adsorption[16]. However it should be noted that wettability is not the only factor mediating protein adsorption. The latter is also susceptible to electrostatic effects and thus is sensitive to the pH of the solution affecting a protein's isoelectric point[17].

Commonly used methods for tailoring wettability include introduction of chemical moieties on the surface and micro/nano fabrication of patterned and textured surfaces[18]. Generally for smooth flat surfaces a maximal water contact angle of around 110º - 120º is attainable[15,19,20]. Beyond this, roughening or surface structuring is required for an increase in contact angle. A well-known example is the so called Lotus effect where surface topography of the

hydrophobic lotus leaves and other plant surfaces enable contact angles of >150º and low sliding angles[21].

Whilst many studies have focused on the engineering of surfaces to mimic nature and on the effects of topography and chemistry, the mechanisms involving the simultaneous effects of both chemical and topographical modification on wettability are not completely understood. However, with further research directed towards this area, applications in biodevices and microfluidic systems stand to benefit from fabrication schemes involving methods for tailoring wettability on surfaces.

A few recent studies on evaluating cell adhesion and wettability on graded surfaces have focused preparation of surfaces with a continuously varying chemical composition along one direction or dimension on the surface[22,23]. These chemical gradient systems produce surfaces with varying properties in wettability, polymer thickness and other physicochemical aspects across one dimension. The advantages conferred in such systems have found use in controlled motion of droplets on surfaces as well as selective biomolecule adsorption for biomaterial design[24]. With the integration of suitable analytical techniques, gradients are powerful analytical tools for examination of a spectrum of effects within a single sample surface.

In recent years, improvements in pSi chemistry and fabrication techniques enable us to tailor pSi surfaces with topographical features spanning from several microns to a few nanometers[1,2]. Dimensions of the porous micro-architecture and the thickness of the porous layer from the silicon wafer can be varied with the anodic etching current density in x, y direction and the time of anodisation in the z direction.

The correlation between of pore size and current density also render pSi attractive as a candidate for studying gradients. The possibility of fabricating pSi gradient surface containing a distribution of pore sizes by anodisation in an asymmetrical setup has been described previously[25]. The current within the electrolytic solution varies as a function of distance of the electrode to the counter electrode due to resistance of the electrolyte, thus leading to a decrease in current density as the distance from the electrode increases[25,26]. This dependence can be exploited to generate a surface displaying a gradient of pore features ranging from large (1-3 μm) to small (5 nm) on a single surface[2]. Modification of the applied anodic current can control the size range of these pores. So far, such lateral gradients have been utilised for the fabrication of optical band filters[27], the studies of biomolecule adsorption[28] and cell-surface interaction[2].

On a typical flat surface, the main influencing factor on wettability will be the nature of the surface chemistry and surface energies. As surface energy is lowered, the hydrophobicity and thus the water contact angle of a surface increases[20]. When a porous surface is introduced in concert with appropriate surface chemistry, the resulting contact angle on the surface will be the net of both factors. Under certain conditions Cassie-Baxter or Wenzel wetting behaviour is observed[12].

In the Wenzel's model, the contact angle on a porous surface can be expressed as the following equation[29,30],

$$\cos \theta_r = r \cos \theta_e \qquad (1)$$

where θ_r serves as a function of the contact angle on a rough surface, θ_e is the contact angle of the droplet on a flat surface and r is the surface roughness. In general, the Wenzel's equation predicts that the wettability of a surface will be enhanced by roughness. In this equation, when the roughness on a surface $\theta_e > 90°$, the equation predicts larger angle change while roughness on a surface with $\theta_e < 90°$ will result in a smaller angle change[30].

The Cassie-Baxter model for a porous material can be expressed in the following equation[29,30],

$$\cos \theta_r = f_1 \cos \theta_e - f_2 \qquad (2)$$

where f_1 is the fraction of fluid area in contact with the material while f_2 is the fraction of fluid area in contact with the air in pores. Whilst the Cassie-Baxter model assumes that a water droplet rests only on top of the surface features without filling pores, Wenzel's model assumes that the surface structure is filled by the water[12].

In this first section of the chapter, we report the ability to tailor wettability across a surface using lateral porous silicon (pSi) gradients. Lateral pore gradients made by anodisation of silicon using an asymmetric electrode configuration displayed a lateral distribution of pore sizes, which decreased with increasing distance from the electrode. Pore sizes were characterised using scanning electron microscopy (SEM) and atomic force microscopy (AFM). Pore diameters ranged from micrometres down to less than 10 nanometres. Chemical surface modification of the pSi gradients was employed in order to produce gradients with different wetting or non-wetting properties. Surface modifications were achieved via silanisation of oxidised pSi surfaces introducing functionalities including

polyethylene glycol, terminal amine and fluorinated hydrocarbon chains. Surface modifications were characterised using infrared spectroscopy. Sessile drop water contact angle measurements were used to probe the wettability in regions of different pore size across the gradient. For the fluorinated gradients, a comparison of equilibrium and dynamic contact angle measurement was undertaken. The fluorinated surface produced gradients with wettabilities ranging from hydrophobic to near super-hydrophobic whereas pSi gradients functionalised with polyethylene glycol showed graded hydrophilicity. In all cases investigated here, changes in pore size across the gradient had a significant effect on wettability.

4.1.1 Methods and material

4.1.1.1 Etching procedure

pSi samples were prepared from p-type (boron-doped) silicon wafers with (100) orientation and resistivity of 0.0005-0.001 Ω cm (Virginia Semiconductors). Samples were prepared in the setup similar to that as previously described[2,25,27]. Briefly, surfaces were etched by placing the electrode perpendicular to the surface (approximately 2 mm from the surface of ths silicon wafer) on one end of a Teflon well (15 mm wide) in a 1:1 (v/v) solution of 49 % aqueous HF/EtOH and applying a constant current for 90 sec (figure 4.1(a)). Three currents were applied: 40 mA, 50 mA and 60 mA over a surface area of 1.767 cm^2. After etching, the samples were rinsed with methanol, acetone and dichloromethane and dried under a stream of N_2. The freshly etched pSi surfaces were thermally oxidised in a tube furnace at 600 °C for 1 h or ozone oxidised using a Fischer OZON Ozon-Generator 500 for 20 mins at ozone rate of 3.25 g h^{-1}. After oxidation, the surfaces were rinsed extensively with EtOH and dried under a stream of N_2.

4.1.1.2 Surface modifications

Surface modifications were achieved via silanisation of the thermally oxidised pSi samples using dry distilled solvent and silanes as received.

Surface modification with N-(triethoxysilylpropyl)-O-polyethylene oxide urethane (PEGS) (Gelest Inc) was achieved by submersion of thermally oxidised pSi in anhydrous toluene with a silane concentration of 50 mM at a temperature of 70^{o}C for 16 h. Modification with 3-aminopropyl triethoxysilane (APTES) (Aldrich, 98 %) was carried out with 50 mM silane in toluene at 25^{o}C for 4 h.

Ozone oxidised pSi was silanised with heptadecafluoro-1,1,2,2-tetrahydrodecyl dimethylchlorosilane (HDFS) (Gelest Inc) and pentafluorophenyl dimethylchlorosilane (PFPS) (Gelest Inc) by incubating the pSi surfaces with the neat chlorosilane in an 80 ^{o}C oven for 15 minutes. After silanisation, the surfaces were rinsed with acetone and dichloromethane before being dried under a stream of N_2.

4.1.1.3 SEM analysis

To visually observe the gradual change in pore sizes on the pSi gradient, SEM analysis was performed on a Phillips XL30 field emission scanning electron microscope with an acceleration voltage of 10 kV and a capture angle of 90 and 45 degrees relative to the surface.

4.1.1.4 AFM imaging

AFM was used to qualitatively measure the dimensions of pore sizes on the gradient and the images were acquired on a Nanoscope IV Multimode microscope (Veeco Corp.) operating in tapping mode using silicon tips (FESP, Digital instruments) with a resonance frequency of

50-70 kHz. Image processing was done using Nanoscope v5.12 software. Analysis was performed in the centre of the respective bins shown in figure 4.1 (b).

4.1.1.5 Diffuse reflectance infrared fourier transform spectroscopy

Analysis of surface chemistry via IR spectroscopy was performed using a Nicolet Avatar 370MCT from Thermo Electron Corporation equipped with a Smart Diffuse Reflectance Accessory in diffuse reflectance mode (DRIFT). The DRIFT spectra were recorded and analysed using OMNIC version 7.0 software. Spectra were obtained in the range of 650-4000 cm^{-1} at a resolution of 1 cm^{-1}. All spectra were referenced to an unetched silicon wafer of the same type as background.

4.1.1.6 Contact angle measurements

To investigate the surface wettability of modified pSi gradients at regions of different pore size, sessile drop water contact angles were characterised in terms of advancing and static (equilibrium) contact angles. Contact angle experiments were conducted under ambient conditions.

A custom built sessile drop apparatus with an Olympus SZ-PT microscope and lens system mated to a Sony CCD camera was employed. A 10 µL syringe (Hamilton, Reno, USA) was used to dispense droplets of 18.2 MΩ.cm MilliQ (MQ) water of approximately 1 µL to three

pore size regions (bins). A minimum of three contact angle measurements were taken from each of the binned regions as described below. Angle analysis of captured droplets was performed with ImageJ software v1.34 (http://rsb.info.nih.gov/ij/).

4.1.2. Results and discussion

4.1.2.1 Asymmetric anodisation of silicon

Graded pSi surfaces were produced using three different etching currents, 40 mA, 50 mA and 60 mA in an asymmetric electrode configuration. The schematic of the setup is as shown in figure 4.1(a). We used three different etching conditions in order to fabricate a spectrum of pore sizes for the wettability studies ranging from micron to nanometer size. A low concentration of HF was selected since this electrolyte gave mechanically stable pores across the whole gradient. The size of surface pores had to be sufficiently large enough to present substantial topographic disparity in conjunction with the chemical modification. A surface topography within the nanometer range may not exert sufficient physicochemical effects on wettability. The physical appearances of the laterally etched pSi surface that we obtained were found to be similar to those previously attained by Sailor's group[25]. For all currents used in this work we were able to avoid electropolishing of the surface. However, any further increase in the etching current resulted in the loss of porous structure due to electropolishing.

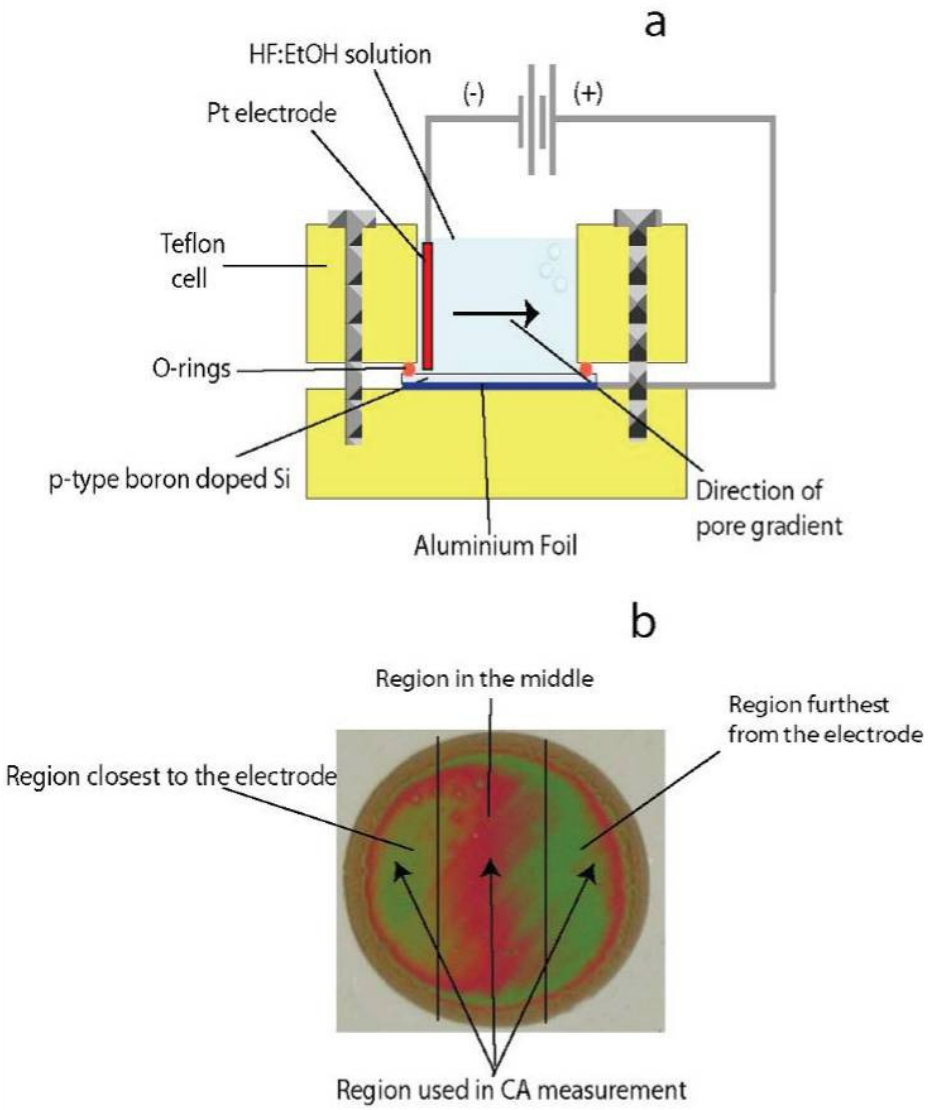

Figure 4.1 - (a) Schematic of setup for production of pSi gradients. (b) Photograph of a pSi gradient with three pore size regions used for sessile drop water contact angle measurements.

4.1.2.2 Surface topography

The topography of the graded pSi films was first characterised using AFM. For this purpose, pSi films etched at the three different currents were divided into different regions as shown in figure 4.1(b). The region nearest to the Pt electrode would be expected to yield the largest pore sizes due to the largest electrical field. Average pore sizes are expected to decrease with increasing distance to the Pt electrode.

Figure 4.2(a)-(c) illustrates the surface analysis on the three different regions of the pSi surface etched at 40mA. At the region closest to the electrode, figure 4.2(a), the pore sizes were found to be between 50-100 nm. In the region approximately in the middle of the surface, the pores were found to be between 20-50 nm (figure 4.2(b)) and in region furthest away from the electrode source, pore sizes were approximately 5-20 nm. The pore size regions for three different applied currents (40, 50 and 60 mA) are shown in Table 1.

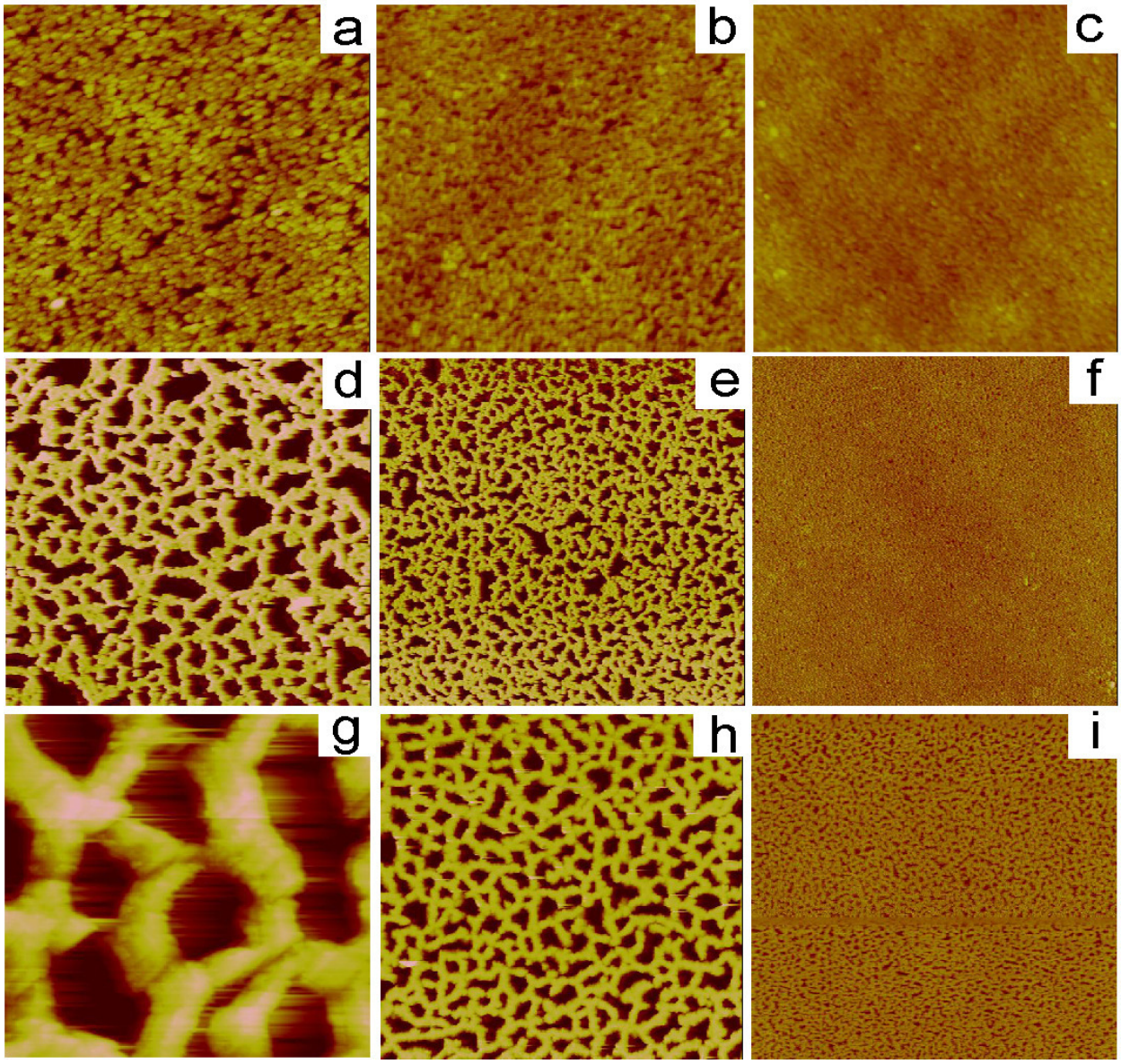

Figure 4.2 - AFM images of pSi etched at (a-c) 40 mA, (d-f) 50mA and (g-i) 60 mA anodisation current. AFM images in a,d,g correspond to the region closest to the Pt electrode, b,e,h correspond to the central region and c,f,i to the region furthest away from the Pt counter electrode. Lateral scale for (a-c) is 1 µm while (d-i) is 5 µm. The z-scale for (a-c) is 10 nm; (d-f) 50 nm; (g-i) is 100 nm.

In general, sizes of pores on the surface were found to be dependent on the distance from the electrode and the level of anodising current applied. The region closest to the electrode was found to have the largest pores while pores were smallest in regions furthest from the electrode.

Table 1 - Pore size distribution on the asymmetrically anodised pSi films for different applied anodisation currents			
Current (mA)	Region closest to the Pt electrode	Middle region	Region furthest from the Pt electrode
40	50-100 nm	20-50 nm	5-20nm
50	300-600 nm	100-300 nm	30-100nm
60	1000-3000 nm	300-1000 nm	70-300nm

Table 1. Pore size distribution on the asymmetrically anodised pSi films for different applied anodisation currents

Since it was impossible to simultaneously determine and differentiate pore size (below 600 nm) visually on the surface during our experimentations, we decided to select six different regions from the three pSi samples corresponding to six different pore size bins to facilitate the analysis of wettability. The bins chosen were 1000-3000 nm, 300-1000 nm, 100-300 nm, 50-100 nm, 20-50 nm and 5-20 nm. This binning method is coarse enough to allow the use fiducial markers to identify the pore size and provides enough film area per bin to obtain sufficiently high good contact angle analysis. Although finer bins could have been selected, the six chosen bins here covered the highest pore size (3000 nm) to the smallest pore size (5 nm) and provided a starting point for evaluating the effect of pore size on wettability.

SEM was performed on all the surfaces to investigate the layer thickness and to further visualise the three dimensional features of the pSi surface that cannot be probed by AFM. Characterisation of the prepared surface structures is important due to the strong influence of topography over the contact angles in conjunction with the chemical silanisation. Figure 4.3(a)-(c) shows the scanning electron micrographs of surfaces produced at 40, 50 and 60 mA, respectively. The thickness of the porous layer was determined to be 2.5 μm from figure 4.3(d) which was taken at a viewing angle of 45 degrees. It is also interesting to note that smaller pore structures were clearly visible along the bottom of the large pores for the 60 mA

samples (figure 4.3(e)). It is conceivable that this layer of smaller pores also influences wettability, in particular for Wenzel surfaces where the water probes the interior of the pore.

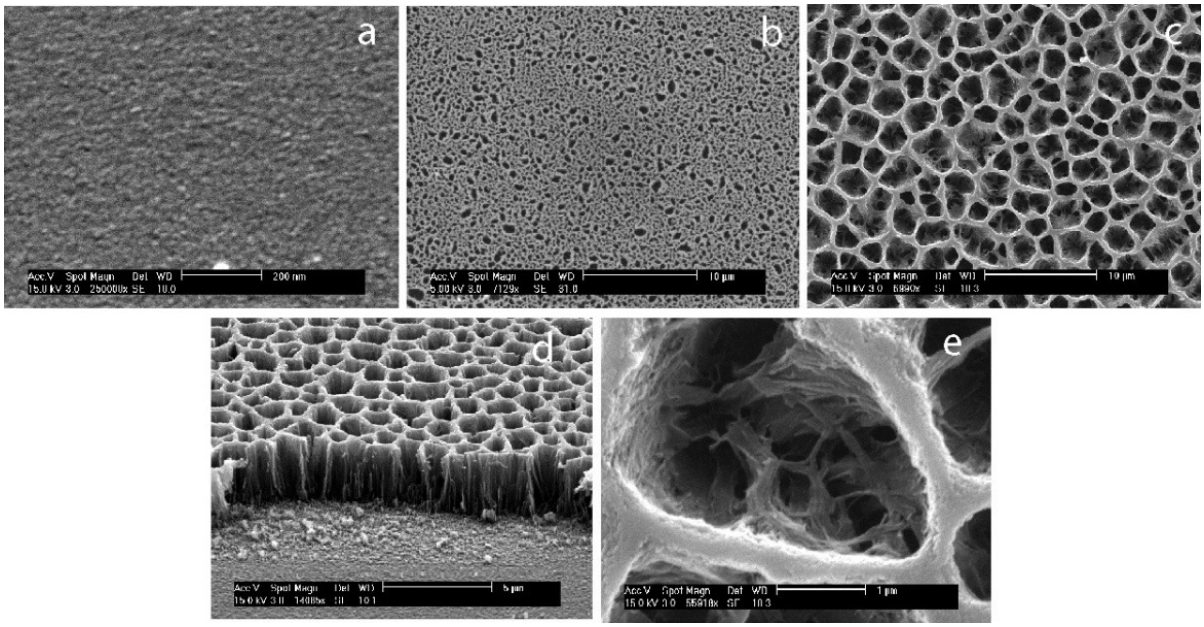

Figure 4.3 - Scanning electron micrographs of gradients for porous silicon produced at (a) 40 mA, (b) 50 mA, and (c) 60 mA etching current. (d) Partly removed pSi layer produced at 60 mA etching current showing a thickness of approximately 2.5 µm. (e) Honeycomb-like microstructures found within individual pores for 60 mA current density. All images are taken from the region nearest to the Pt electrode.

4.1.2.3 Surface modifications

pSi gradients were oxidised to produce a surface that is stable when in contact with aqueous media[2]. Thermally oxidised pSi was silanised with the silanes N-(triethoxysilylpropyl)-O-polyethylene oxide urethane (PEGS)[2] and with 3-aminopropyl triethoxysilane (APTES)[31] to produce two hydrophilic organic coatings. On the other hand, ozone oxidised pSi was silanised with fluorinated silanes heptadecafluoro-1,1,2,2-tetrahydrodecyl dimethylchlorosilane (HDFS) and pentafluorophenyl dimethylchlorosilane (PFPS) to produce two hydrophobic coatings[32].

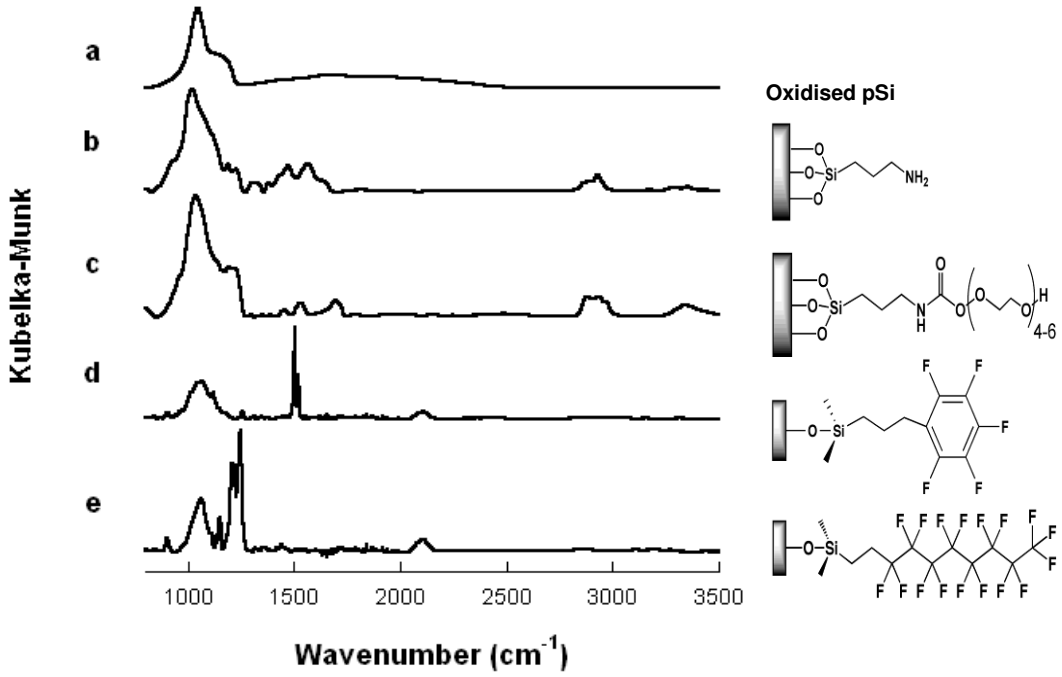

Figure 4.4 - DRIFT spectra of (a) thermally oxidised pSi, (b) APTES silanised pSi, (c) PEGS pSi, (d) PFPS pSi and (e) HDFS pSi. The corresponding surface functionalities are also displayed.

Typical IR spectra for each surface functionalisation are shown in Figure 4.4. Upon thermal oxidation, the laterally etched surfaces (Figure 4.4 (a)) show a characteristic peak at 1080 cm^{-}

[1] corresponding to a Si-O stretching vibration[33]. The APTES pSi surface (figure 4.4 (b)) displays a large peak at 1080 cm^{-1} for the Si-O stretching as well as a broad peak corresponding to an N-H bending vibration centered at around 1580 cm^{-1}. C-H stretching vibrations at 2850 – 3000 cm^{-1} and a peak corresponding to the bending vibrations at 1460 cm^{-1} are also observed. The PEGS silanised surface (figure 4.4 (c)) shows a broad peak at around 1080 cm^{-1} for the Si-O and C-O stretching vibrations. The spectrum also shows characteristic peaks at 1460, 1545 and 1710 cm^{-1} for the C-H alkane and N-H amide bending and the C=O stretching vibrations in the amide, respectively. A peak corresponding to C-H stretching vibrations can also be seen at 2850 – 3000 cm^{-1} along with a small broad peak around 3400 cm^{-1} which can be attributed to the terminal O-H group on the PEGS pSi.

Both the PFPS (figure 4.4 (d)) and HDFS pSi (figure 4.4 (e)) surfaces also show peaks centered at 1080 cm^{-1} for the Si-O stretching, and the symmetric stretching vibration of CF_3[34]. Importantly the PFPS pSi spectrum (figure 4.4 (d)) shows a peak at 1260 cm^{-1} which can be attributed to aromatic C-F stretching vibrations and peaks at 1500 cm^{-1} attributed to the C-C in ring stretching vibrations of aromatic systems. The HDFS pSi spectra (figure 4.4 (e)) clearly shows sharp peaks that can be assigned to CF_2 stretching vibrations at 1150 and 1220 cm^{-1} and the CF_3 asymmetric stretching vibration at 1250 cm^{-1} [34]. Due to the low sensitivity of diffused reflectance IR on laterally graded porous surfaces, it is hard to observe any C-H stretching vibrations on both the HFDS and PFPS pSi surfaces. However these surface appear to contain residual Si-H bonds judging by the presence of a small peak at 2100 cm^{-1}, which is representative of Si-H_x stretching vibrations. This indicates incomplete ozone oxidation.

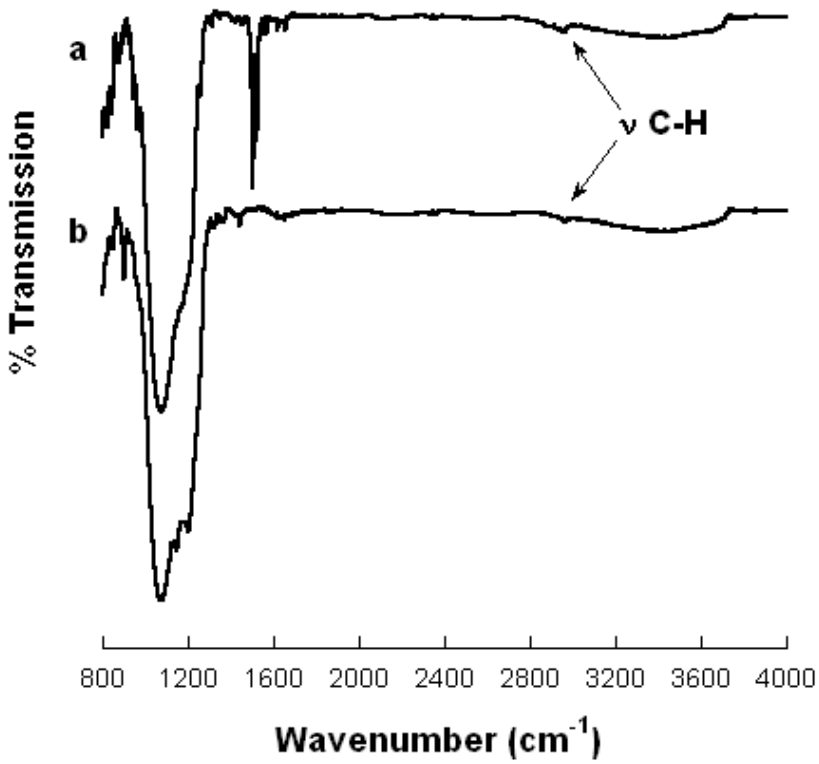

Figure 4.5 - Transmission IR spectra of pSi silanised with (a) PFPS and (b) HDFS.

Transmission IR scans measurements were also attempted, in order to visualise the C-H stretches for the short propyl chains and to further confirm the successful surface functionalisation with both PFPS and HDFS. In order to facilitate the transmission of the IR beam through the samples, higher resistivity (3-6 Ω cm) boron doped silicon wafers were etched at a current density of 60 mA for 150 seconds, ozone oxidised and silanised with PFPS and HDFS, respectively. The results are shown in figure 4.5 and the C-H stretch indicated by a peak at 2960 cm^{-1} is visible in these spectra. It is important to note that all the peaks assigned for both PFPS and HDFS from the DRIFT spectra (figure 4.4 (d)-(e)) were also visible in transmission mode IR as expected. The large peak at 1080 cm^{-1} is attributed to the Si-O stretching vibration from the surface and is much more prominent on these surfaces, whilst the Si-H vibrations are absent in the spectra, indicating complete ozone oxidation in these cases.

4.1.2.4 Water contact angle measurements

Static water contact angles were determined on pSi gradients with the surface modifications as shown in figure 4.6 to study the effect of pore size on wettability for hydrophilic (PEGS and APTES pSi) and hydrophobic (PFPS and HDFS pSi) coatings. The results are shown in figure 4.6 and 4.7.

Figure 4.6 shows digital photographs of 1µl water droplets on three pore size regions, 300-1000 nm, 100-300 nm and 5-20 nm on PEGS, PFPS and HDFS pSi. The fluorinated surfaces PFPS and HDFS pSi demonstrate low wetting in general and an increased beading of the water with increasing pores size (figures 4.6 (a)-(c) and 4.6 (d)-(f)).

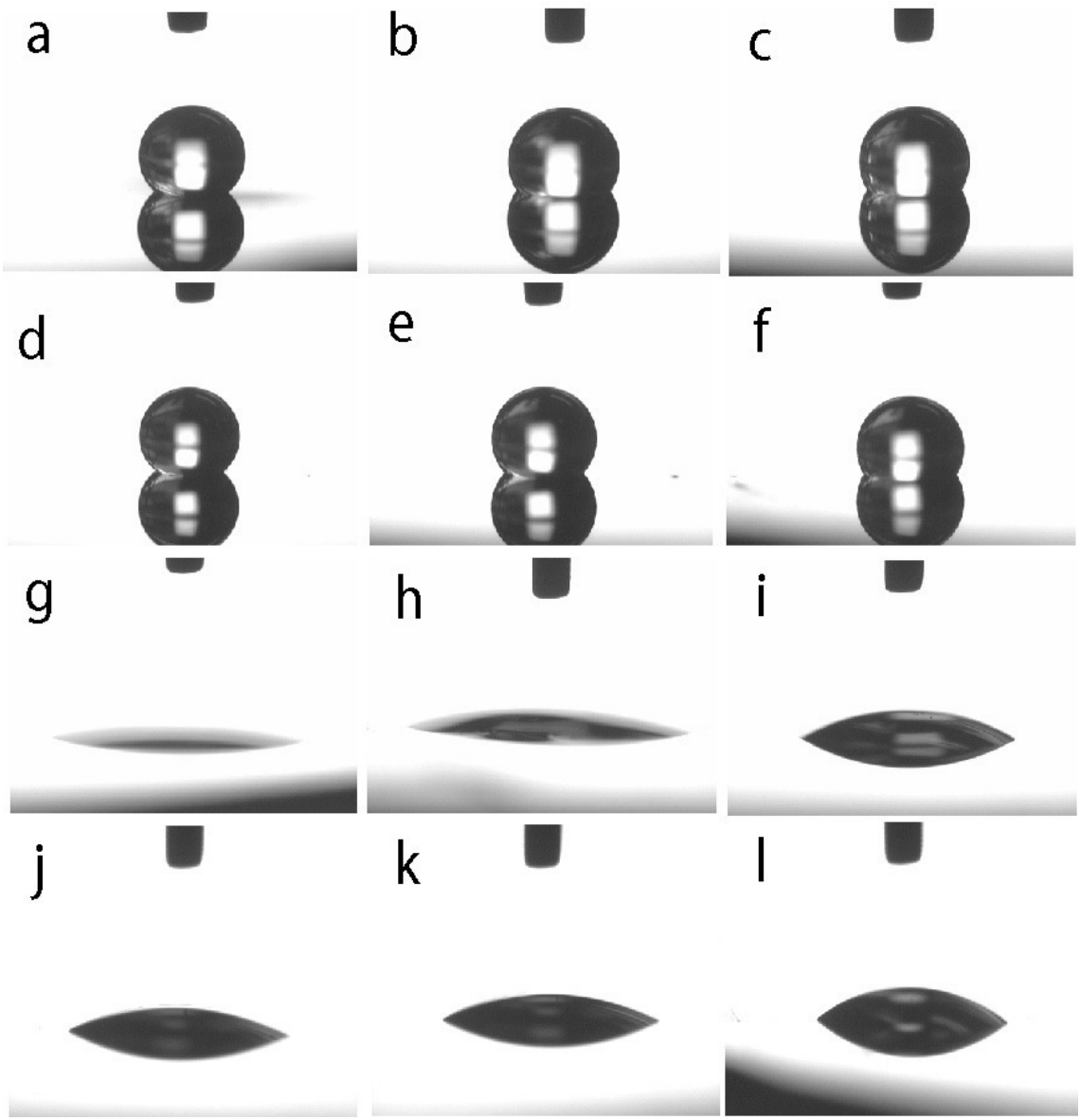

Figure 4.6 - Photographs of static water contact angle measurements performed on different surfaces corresponding to three binned pore size regions, with the largest pores from the left to the smallest pores from the right for PFPS (a) 1000-3000 nm, (b) 100-300 nm and (c) 5-20 nm, for HDFS on (d) 1000-3000 nm, (e) 100-300 nm and (f) 5-20 nm, for PEGS on (g) 1000-3000 nm, (h) 100-300 nm and (i) 5-20 nm and for ATPES (j)1000-3000 nm, (k) 100-300 nm and (l) 5-20 nm. PEGS and APTES functionalised surface shows an increase in contact angle with decreasing pore size while both PFPS and HDFS pSi displayed the reverse trend.

The hydrophilic PEGS functionalisation shows the reverse trend to the fluorinated porous surfaces with droplet flattening as pore size increases. Therefore in all cases studied here, the larger pore sizes enhance the effects of the applied surface chemistry.

Figure 4.7 shows the average static water contact angles for the six pore size regions in figure 4.2. The fluorosilanes produced hydrophobic surfaces with contact angles in excess of 112º (figure 4.7 (a)). Small standard deviations of less than 2.5º for both PFPS and HDFS coatings are indicative of homogenous coatings. A difference of approximately 11º is observed for the between the smallest and largest pore sizes for both PFPS and HDFS pSi. Values for HDFS pSi are slightly larger than for PFPS pSi which is within expectations as the surface energies for a HDFS coating displaying a terminal CF_3 group is lower than for a PFPS coating[35]. The highest contact angles (around 125º) were observed on the micron size pore regions. On the 5-20 nm pore region, the contact angles were around 113º. In contrast, the static contact angle on flat Si modified with PFPS and HDFS was 90º and 100º, respectively, which is significantly lower than the values obtained on the mesoporous region (5-20 nm).

It is a well established fact that surface roughness and topography on an already hydrophobic surface can further augment hydrophobicity[29, 36, 37]. The trend we observed on the fluorinated surfaces as described above shows a decrease in contact angle from the largest pores to the smallest one. Based on the Cassie-Baxter model, the contact angle on a composite surface composed of solid material and air (e.g. a porous surface) increases when the fraction of the liquid-air interfacial area increases[38]. The higher the porosity, the higher the fraction of liquid-air interfacial area. This model therefore explains well the trend observed here. Previous studies on porous fluoropolymer films templated by silica colloidal assembly with

similar pore size ranges show comparable trends[39]. Our failure to attain superhydrophobicity could be due to the incomplete coverage of the fluorosilanes on the surface and this will be addressed in future work. Interestingly, earlier studies on chemically modified CF_3 flat surfaces were only able to achieve a contact angle of 120º[35, 40], while here the lateral gradient has clearly demonstrated the enhancement of hydrophobicity, with the highest contact angle obtained at 125º .

A difference in contact angle of 27º between the smallest and largest pore size regime was observed for the PEGS functionalised gradients (figure 4.7 (b)). The lowest contact angle observed was 17º (on the 1000-3000 nm region) and the largest 44º (on the 5-20 nm region). These results indicate that the hydrophilic coating allows the water droplet to fill the internal volume of the porous structure observed in figures 4.2 and 4.3. Investigation of the static contact on flat Si modified with PEGS showed a slightly higher contact angle of 47º, which is consistent with the trend observed. Whilst APTES functionalised surfaces follow the same trend as PEGS pSi, the change in contact angle is less pronounced. A difference of 9º between the smallest and largest pore size areas for the APTES samples is observed. The standard deviation of contact angles is larger for the APTES functionalised surfaces, perhaps due to a more inhomogeneous coating. APTES has a tendency to form a polycondensed multilayer[41]. Taking the large standard deviation into account, it can be concluded that the pore size changes do not as strongly influence wettability of APTES pSi as compared to the PEGS surfaces.

The wettability trend on the hydrophilic porous gradient can be explained by the Wenzel model. In this model, if a porous microstructure is readily invaded by water, an increase in the solid-liquid surface area (e.g. by decreasing pore size) will augment hydrophobicity

because of an increase in surface energy of the porous surface[29]. An increase in the absorbed volume of water (e.g. by increasing pore size) however leads to an increased hydrophilicity. Surface silanisation with PEGS and APTES creates hydrophilic surfaces, which should allow the penetration of the water droplets into the pores. The larger the pore volume, the more water of the droplet can be absorbed into the porous surface (nanowicking)[42-44]. This explains the observed increase in wettability for increasing film porosity.

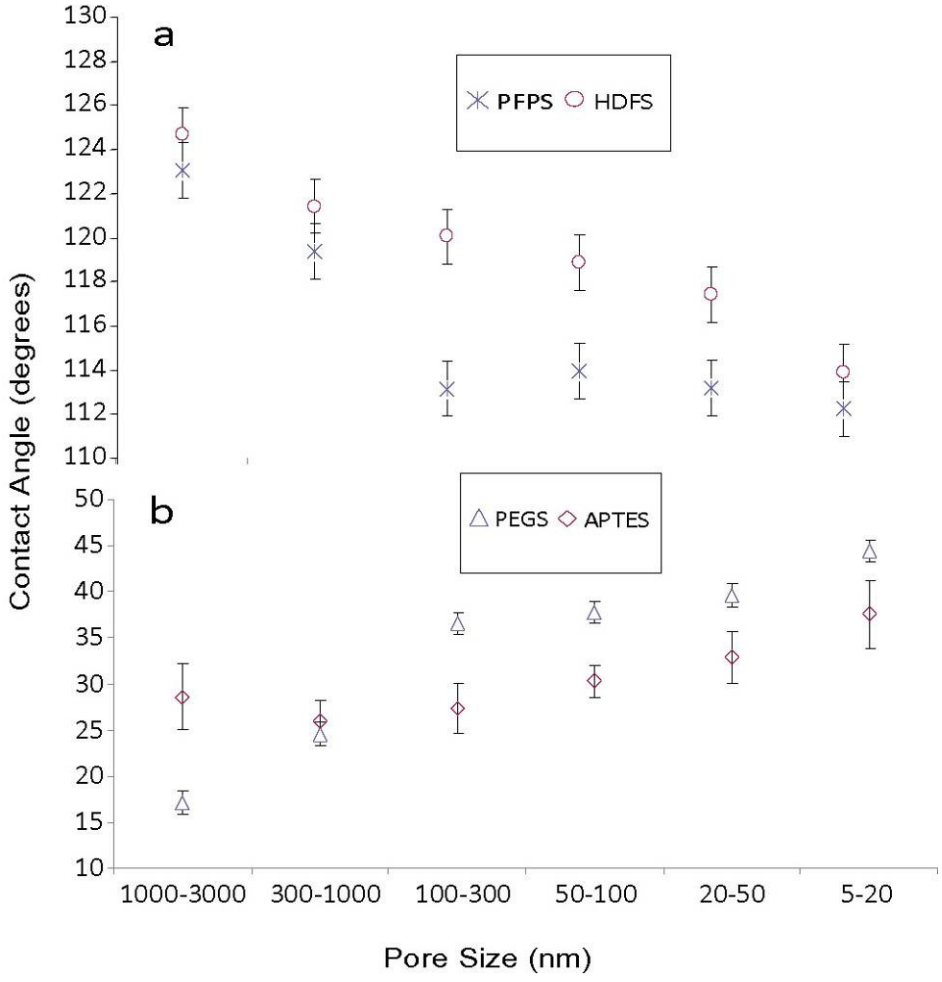

Figure 4.7 - Static water contact angles on (a) PFPS or HDFS functionalised pSi gradients and (b) PEGS or APTES functionalised pSi gradients. The change in contact angle over the lateral gradient on hydrophilic surfaces for PEGS and APTES was 27º and 9º, respectively. The changes on hydrophobic silanes for both PFPS and HDFS were found to be relatively similar, at approximately 11º. All contact angle measurement were performed in triplicates.

When dynamic advancing contact angles were measured for the hydrophobic surfaces (PFPS and HDFS), a stronger dependence of the wettability on the pore size was observed. Figure 4.8 shows the advancing contact angle for the HDFS functionalised samples. It can be seen that the difference between the maximal 147º and minimal 114º contact angle values for the largest and smallest pore sizes respectively, was now 33º whilst the static contact angle difference was only 11º. This difference between the advancing and static contact angles is clearly caused by the introduction of a porous layer, where an increase of surface roughness greatly enhances its hydrophobicity and thus reduces surface affinity during water contact[35]. In contrast, the advancing contact angle of flat Si sample modified with HDFS (98º) was very close to the static contact angle of HDFS on flat Si (100º). The upper value of 147º is approaching the superhydrophobic regime, which is usually defined as a regime of contact angles in excess of 150º[36].

Pore sizes	**PEGS (experimental)**	**APTES (experimental)**	**Calculated values**
1000-3000 nm	17º	28º	23º
300-1000 nm	26°	24°	37°
100-300 nm	36°	26°	41°
50-100 nm	37°	29°	44°
20-50 nm	38°	32°	45º
5-20 nm	44º	35º	47º

Table 4.2 – Measured CA values on the different pore sizes on the hydrophilic surfaces and the calculated values based on the Wenzel equation.

Table 4.2 shows the predicted values derived using the Wenzel model (equation 1) for the different pore sizes. For the hydrophilic surfaces, as the pore size decreases on the surface, the calculated CA values from the equation increases. This trend in CA change corresponds relatively well to our experimentally derived values. However it is interesting to note that our

measurements were much lower than those derived from the equation, especially for the surfaces functionalised with the PEG silane and can be attributed to the presence of hydrophilic moiety on the surface of the pSi.

Pore sizes	PFPS (experimental)	HDFS (experimental)	Fraction of pores in contact with solution	Calculated values
1000-3000 nm	123º	125º	49.7%	120º
300-1000 nm	119°	121°	32.7%	83°
100-300 nm	113°	121°	24.9%	75°
50-100 nm	114°	120°	11.9%	62°
20-50 nm	113°	118°	4.3%	53º
5-20 nm	112º	114º	0.5%	52º

Table 4.3 – Measured CA values on the different pore sizes on the hydrophobic surfaces and the calculated values based on the Wenzel equation.

On the hydrophobic surfaces, we compared our experimentally derived values to those calculated from the Cassie Baxter equation. As shown in table 4.3, our CA values were much higher than calculated and the trend of CA reduction was not observed as the pores become smaller. This can be explained by the fact that the equation only takes unmodified surfaces into consideration while our surfaces were functionalised with hydrophobic silanes. This functionalisation help improve the water repellent nature of the areas that were in contact with the droplet in conjunction with the air pockets on the surface and that surface attribute can also help explain why the surface remain fairly hydrophobic even at lower pore sizes.

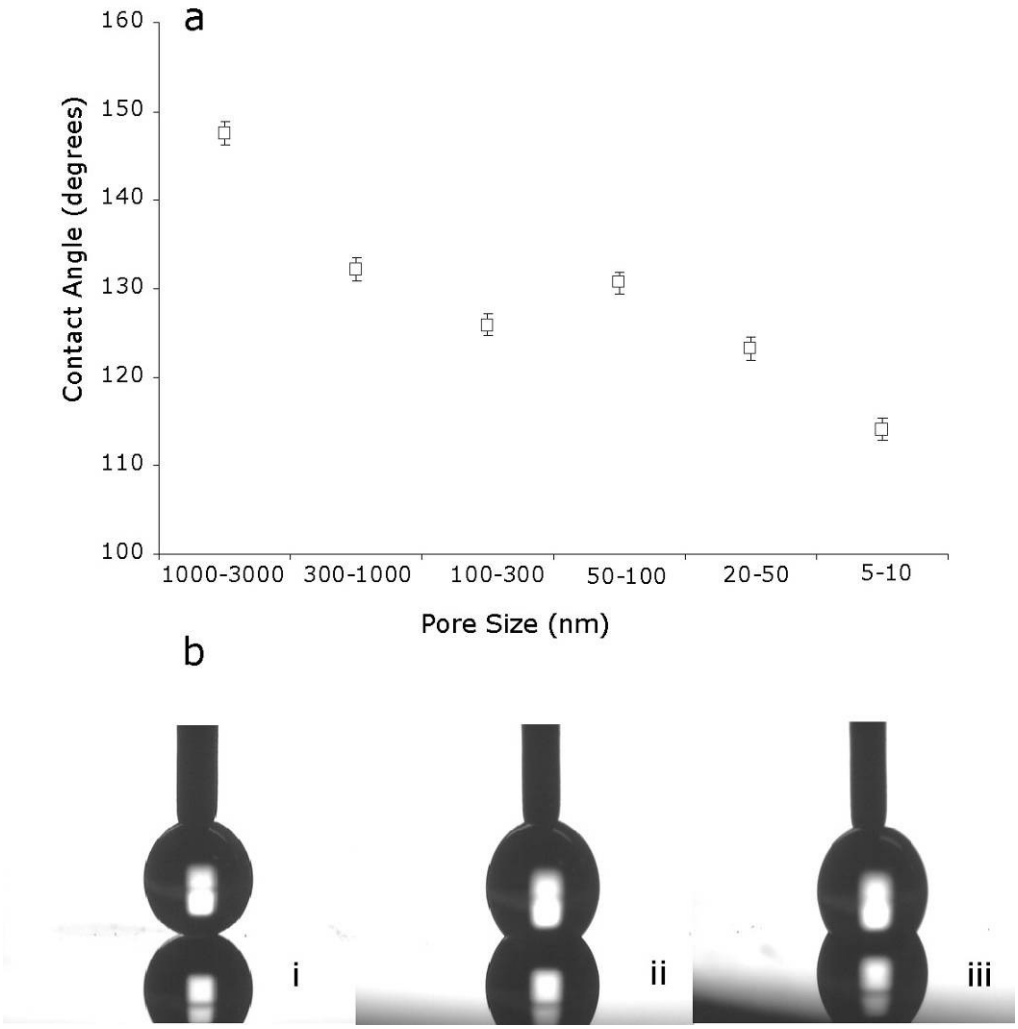

Figure 4.8 - (a) Graph of advancing water contact angle measurements on HDFS functionalised pSi. (b) Photographs of advancing water contact angle experiments performed on (i) 1000-3000 nm, (ii) 100-300 nm and (iii) 5-20 nm pore size regions of HDFS functionalised pSi. The change in contact angle between the largest and the smallest pore region is 33º. Advancing contact measurements were performed in triplicates.

The fluorinated pSi gradients showed a contact angle hysteresis of 22º. The large contact angle hysteresis is indicative of a strong pinning of the liquid-solid contact line and a 'sticky' hydrophobic surface[45]. At this point, the reasons for the large hysteresis are uncertain. It may be a consequence of the graded nature of the surface or may be related to the dispersity of the pore size and shape.

4.1.3. Conclusions

We have developed gradients with micro/nano structured surface features which are amenable to surface functionalisation via silanisation. Lateral pSi gradients were prepared by an electrochemical etching procedure using an asymmetric electrode configuration. Simple one step surface modifications of the pSi using silane chemistry afforded surfaces with a range of wettabilities as probed by the sessile drop water contact angle from less than 20º to approximately 150º. For a given surface chemistry, pore size changes of these pSi gradients result in shifts of water contact angle of around 30º.

Depending on the surface chemistry, we have attributed these wettability behaviours to the Wenzel or the Cassie-Baxter model. With further utilisation of both models, we have also managed to determine the relationship between pore size and wetting behaviours on porous substrates.

Hence, using this gradient format, one can identify desired wettability regimes on a single sample therefore reducing analysis and preparation cost and time. The format is also suitable for the investigation of biomolecule surface or cell surface interactions with the aim to develop surfaces with desired surface properties for biotechnological applications including biomaterials, biosensors and microarrays.

4.2. Using continuous porous silicon gradients to study the influence of surface topography on the behaviour of mammalian cells

The understanding of substrate surface induced morphological and metabolic changes to cells or tissue is of enormous importance to the fields of biomaterials and tissue engineering[46, 47]. As cells are often in direct contact with a substrate surface, substrate topography[48, 49], hydrophobicity[50-52] and surface chemistry[53-55] are certainly expected to influence the cell behaviour. In particular, the shape, morphology and orientation assumed by cells upon contact with a substrate surface can be influenced by the physical cues presented to the adherent cells. Chemical and biological cues presented to the adherent cells for example in the form of immobilised extracellular matrix proteins are known to allow the control of cell behaviour[56-58]. But knowledge gained from studies focusing on the response of cells to physical cues including topography and material stiffness portends the control of cell behaviour in the absence of biological signals.

The investigation of substratum effects on cells was first conducted more than 90 years ago[59]. The concept of "contact guidance" was introduced by Weiss in his studies of nerve cells using plasma clot[60] and glass fibres[61] as substratum. In recent years, many well-executed studies on the effects of contact guidance have emerged using a wide selection of surface topographies[48, 62-65]. However, the feature dimensions on these surfaces were mainly on micron and submicron scales and the features themselves were ordered, i.e parallel groves etc. Since the typical width of an adhering mammalian cell on a substratum ranges from 10 µm to 30 µm, it is easy to comprehend that changes to surface topography on the micron scale will influence cell morphology.

The advent of various enabling technologies in surface chemistry and nanotechnology has made it feasible to fabricate surface texture and topography down to the nanometer range in the form of gradients[25, 66]. Such topographical gradients have the potential to reduce sample numbers and therefore analysis time in comparison with the conventional one data point-one sample analysis. pSi is a particularly promising candidate for the fabrication of such graded nanostructures. Apart from being very biocompatible and good tunable pore/surface chemistry (see section 4.1), pSi films can promote cell adhesion and viability[31, 67-69]. Another advantage of this material is that nutrient and metabolite movement/diffusion through the porous layer on which cells reside can potentially enhance longevity of cells in culture[70].

The effects of surface topography on cell behaviour are the subjects of intense research in cell biology. These effects have so far only been studied using substrate surfaces of discretely different topography. Here, we apply the asymmetric anodisation approach of silicon wafers to characterise cell growth on topographical pSi gradients that display pore sizes from several thousands to a few nanometers. This widely applicable format has the potential to significantly reduce sample numbers and hence analysis time and cost.

Following the correlation between pore size, chemistry and wettability in the previous section, the same lateral gradients were used for detailing cell-surface behaviour in this section. The application of pSi gradients for the study of topography-induced changes of morphology was performed for the human neuroblastoma cell line SK-N-SH. This cell line was used here as the cell culture model for predicting the morphogenesis of primary neurons on pSi films which is important for the construction of neuro-electronic junctions[71]. The control of neuronal cell morphology on microelectronic substrates can be exploited in the design of neuronal networks and interfaces for biomedical applications[72]. Neuroblastoma

cells are known to be adhesive to a variety of substrate surfaces[73, 74] and are commonly used as experimental model in neurobiology to study cell differentiation[75, 76], signaling and ion channel function[77-79].

Here, thermally oxidised lateral pSi gradients were produced with pore sizes ranging from the nano- to the microscale as described in the last section. Cell morphology and growth on these surfaces were investigated by means of fluorescence microscopy, laser scanning confocal microscopy and scanning electron microscopy. We observed a dramatic influence of changes in surface topography on the density and morphology of adherent neuroblastoma cells. For example, pore size regimes where cell attachment is strongly discouraged were identified providing cues for the design of low fouling surfaces. On pore size regimes more conducive to cell attachment, lateral cell-cell interactions crosslinked the cell layer to the substratum surface, whilst direct substrate-cell interactions were scarce. Finally, our study revealed that cells were sensitive to nanoscale surface topography with feature sizes of <20nm.

4.2.1. Materials and methods

4.2.1.1 Cell culture

Prior to cell culture, the asymmetrically anodised pSi surfaces (see section 4.1.1.1) were extensively washed with EtOH and dried with N_2 in a laminar flow hood. The pSi wafers were then transferred onto sterile 6-well plates. Before seeding of the cells on the surface, the pSi was incubated with complete DMEM for 10mins. 1ml of SK-N-SH neuroblastoma cells (a gift from Prof. R. A. Rush, Flinders University) at a density of about $6.3x10^5$/ml was then added into each well. The pSi gradients were incubated at 37°C for 24 hours.

4.2.1.2 Cell viability staining

At the end of the incubation time, 10 µl of 15 mg/ml of fluorescein diacetate (FDA) in acetone were added to the media to test for cellular viability. After 10 min of incubation at room temperature, the pSi samples were removed from the wells and gently rinsed with phosphate buffered saline (PBS). Cell attachment was observed using a Leitz fluorescence microscope using an excitation wavelength of 495 nm and an emission of 515 nm.

4.2.1.3 Cell density

SK-N-SH cells were seeded at a cell density of $6.3x10^5$/ml on the gradient surfaces. After 24 hours of incubation at 37ºC, 2 µg/ml of Hoechst 33342 dye was added to the culture wells in order to stain the cell nucleus and the wells were incubated at 37ºC. The surface was

subsequently washed with PBS to remove non-adhering cells. Fluorescence microscopy using an excitation band filter of 270-380 nm was performed and cells were counted on 3 replicate samples for each surface, on an area of 1 mm^2.

4.2.1.4 Laser scanning confocal microscopy (LSCM)

At the end of the incubation time, the cells were incubated with 2 µg/ml of Hoechst 33342 dye for 30 mins before gently rinsing the wells twice with PBS. The cells were subsequently fixed with 3.7% formaldehyde in PBS for 10 mins at room temperature and washed with PBS. After fixation, 5mls of 0.1% Triton X-100 in PBS was added to each well for 5 mins and each well was rinsed again with PBS. 5 µl of 6.6 µM of Alexa Fluor® 594 phalloidin (Invitrogen) was added to 200 µl of PBS and the solution was added into each well and incubated in the dark for 30 mins. The cells were finally rinsed with PBS and stored in 10 % glycerol in PBS and adjusted to pH 8.0 (buffered glycerol) in the dark. Confocal microscopy was performed on a Leica TCS SP5 laser scanning confocal microscope.

4.2.1.5 SEM analysis

For cell fixation, the pSi surfaces were carefully removed from the 6-well plate, rinsed once with PBS and fixed in 3.7% formaldehyde in PBS for 10 mins at room temperature. Subsequently, the surfaces were washed again twice in PBS and incubated in turn in 50%, 75% and 100% EtOH for 10 mins. The surfaces were then washed twice in PBS, incubated in hexane, dried in the laminar airflow, and subsequently coated with platinum. Scanning electron microscopy (SEM) was performed on a Phillips XL30 field emission scanning electron microscope with an acceleration voltage of 10kV.

4.2.1.6 Measurement of cell area and length

Cell area was calculated by using the analySIS LS research program (Olympus Soft Imaging Solutions). Confocal images of stained cells were processed to determine the total area of the image covered by cells. The area per single cell was determined by dividing the total area by the total number of cells (> 50) in the field of view. Cellular length was measured by using the linear measuring tool on the analySIS software upon calibration. A measurement of an average of 10 cells of each region was performed.

4.2.1.7 Statistical analysis

SPSS v.15 (SPSS Inc.) was used to perform a one-way analysis of variances (ANOVA) on the experimentally determined values of cell density, area and length with the different porosity regions as the fixed factor and density, area and length as dependent variables. The ANOVA was performed three times for each of the dependent variables and with $p \leq 0.05$ to be considered as statistically significant. A post hoc analysis using the LSD method was also performed to determine the statistical significance between each of the pore regions.

4.2.2 Results and discussion

4.2.2.1 Lateral pore gradients

Surface topography is a common cues/property experienced by adhering cells. Therefore, a better understanding of the influence of topography on cell behaviour would be of great relevance to biomaterials and tissue engineering[80, 81]. Cellular interactions with the surface are mediated by transmembrane integrin receptors whilst neuronal cell-cell interactions are mediated by processes outgrowth and filopodia[82, 83]. In the presence of well-defined micro- and nanopatterned surfaces, cell substrate surface interactions are redefined forcing the cells to undergo significant morphological changes. Previous studies highlighted the ability of topography to induce significant morphological changes to anchorage-dependent cells independent of the surface chemistry[84-87].

Silicon wafers were etched at three different anodisation currents, 40mA, 50mA and 60mA using the asymmetric electrode configuration described above. The schematic of the setup is similar to that as shown in figure 4.1. The main purpose of utilising three different etching conditions was to vary the properties of the pore gradients and to cover a wider spectrum of pore sizes that can be studied in cell culture. A 1:1 EtOH/HF ratio was selected since etching using this electrolyte composition gave stable pores over a wide pore size range at high porosity (65-85%). The appearance of the resulting laterally graded pSi films was similar to those reported by Collins et. al[1]. However, even at the highest applied current of 60mA we were able to avoid electropolishing of the surface even in the region closest to the Pt counter electrode shown in the optical photograph in figure 4.1 (b). This is an important result since

electropolished, non-porous regions on the film were undesirable for our studies of the influence of porous topographies on cell behaviour.

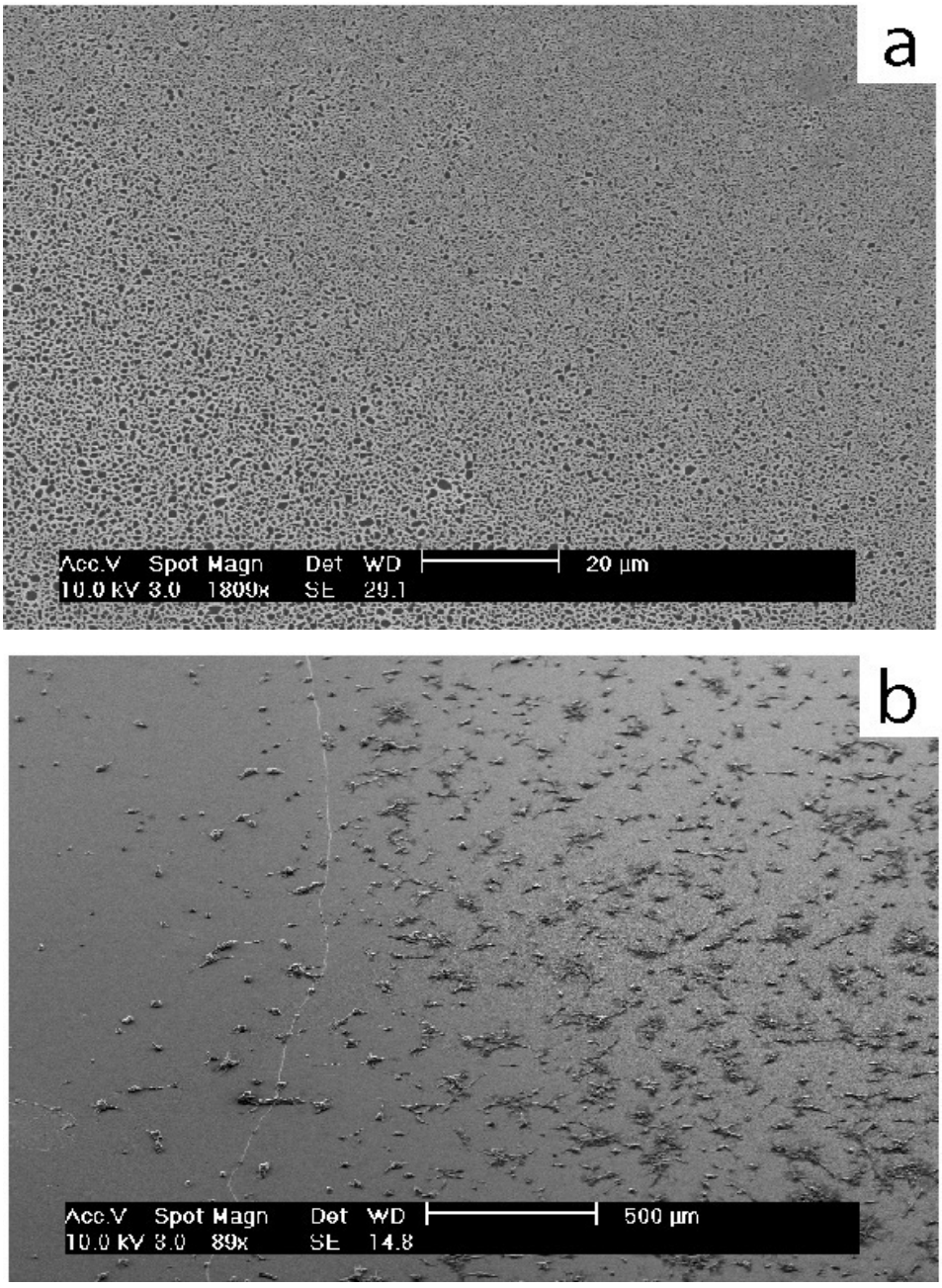

Figure 4.9 - Scanning electron micrograph (SEM) of (a) pSi surface fabricated by asymmetric electrochemical anodisation at a current of 60mA showing a lateral pore size gradient extending across the image. (b) Neuroblastoma cells growing on a pSi gradient. Note the change in cell morphology across the gradient, spanning from 3000nm to 600nm. The white line in the image was etching artefact.

SEM was performed to visualise the introduced topography gradients and to confirm the AFM results. Figure 4.9 (a) shows an electron micrograph of a pSi film prepared at 60mA displaying a lateral pore size gradient from left to right. SEM images of the different regions on the gradient (figure 4.10) corroborated our AFM results (figure 4.2) in terms of pore size.

4.2.2.2 Neuroblastoma cell culture

As an application for our gradient technique, an adherent human neuroblastoma cell line was chosen to study the influence of topographical changes on cell growth parameters. Cell culture on the graded pSi surfaces was performed over 24h to focus on the initial response to the substratum. After 24h incubation, the cells were stained with the cell viability stain FDA and counterstained with Hoechst 33342. The majority of the cells that had taken up the Hoechst dye also showed fluorescein fluorescence confirming the viability of the cells on these surfaces. On the unetched flat silicon, neuronal cells appeared healthy, with well spread processes and exhibited the teardrop shape morphology characteristic of this cell line[88, 89] (figure 4.10 (m)). This typical morphology changes upon contact of cells with six different pore size regions of the laterally graded porous surface. On the 1000-3000 nm pore size region, a woven-like sheet of cells was observed (figure 4.10 (a)) mirroring to some extent the much finer honeycomb structure of the pSi pores. Cell clustering was not observed and cell-cell interactions were often bidirectional resulting in the formation of strings of cells often featuring neuritic processes. For the region between 300-1000 nm, more cell clusters were observed leading to less extensive cell network connectivity (figure 4.10 (c)). While the cells did not lose the characteristic teardrop morphology, the neuritic processes became less frequent. This trend of increasing clustering and less frequent/shorter neuritic processes continued with decreasing pore size. On the 100-300 nm region, patches of clustered cells

were observed and the cell layer no longer showed the honeycomb appearance noted above (figure 4.10 (e)). The formation of cell clusters was even most prominent on the 50-100 nm region (figure 4.10 (g)). Neuritic processes were rare on this region. Interestingly, on the 20-50 nm region, cells formed more frequent processes again (figure 4.10 (i)). On the 5-20 nm pore size region (figure 4.10 (k)), cell morphology was similar to that observed on the non-etched silicon (figure 4.10 (m)).

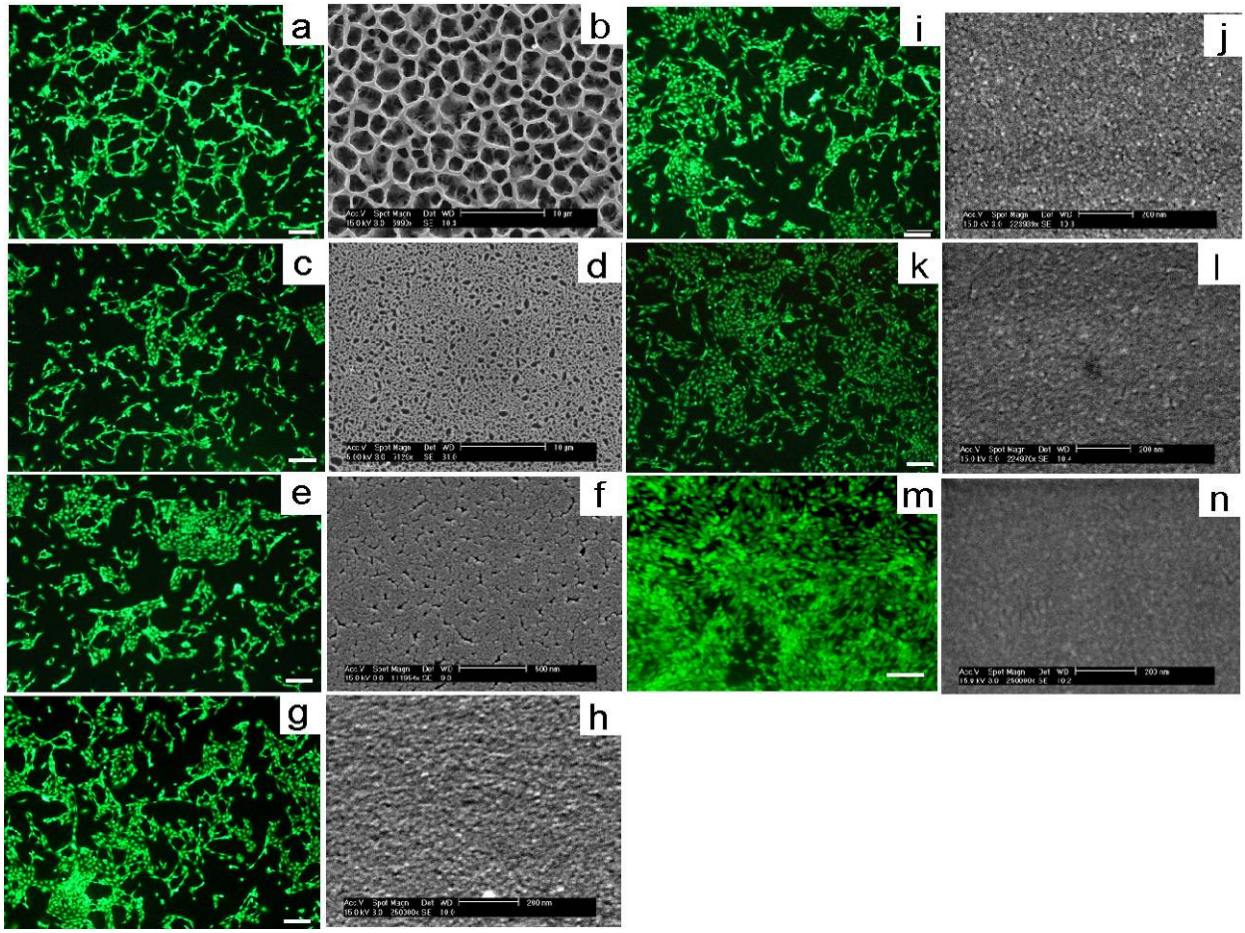

Figure 4.10 - Fluorescence microscopy of FDA stained neuroblastoma cells growing on (a) 1000-3000 nm, (c) 300-1000 nm, (e) 100-300 nm, (g) 50-100 nm, (i) 20-50 nm, (k) 5-20 nm and (m) flat silicon. The corresponding scanning electron micrographs on the right show the typical topography of those regions, (b)1000-3000 nm, (d) 300-1000 nm, (f) 100-300 nm, (h) 50-100 nm, (j) 20-50nm, (l) 5-20 nm and (n) flat silicon. The white scale bar in the fluorescence microscopy images corresponds to 100 µm. All experiments were done in triplicates.

4.2.2.3 Cell morphology

Laser scanning confocal microscopy and SEM were employed to study the effects of porosity on the morphology of single adhering cells and to determine cell size and well as to investigate the organisation of the neuritic processes. Figure 4.11 shows representative images of cells growing on the six different pore size regimes and on flat silicon as a control. Cell nuclei were stained with Hoechst dye, while the cytoskeletal F-actin network was stained with phalloidin tagged with an Alexa Fluor® fluorophore. Neuroblastoma morphology was found to vary significantly on each of the different pore size regions. On the large pore size region, 1000-3000 nm, on average three to four long processes with well-spread ends were observed protruding from the main cell body. The cell bodies themselves were ovoid and slightly raised above the substratum (figure 4.11 (a)-(b)) minimising contact with the surface. The diameter of the main cell body growing on this surface was in general much larger, about 20-40 µm in diameter in comparison to the 10-15 µm normally associated with the size of adhering neuroblastoma cells[88, 90]. As such, individual cells appeared to be much larger than others growing on regions of smaller pore size. On the region displaying pores of 300-1000 nm diameter, the cellular processes were significantly shorter, yet cell bodies appeared again ovoid to ellipsoid and were raised conspicuously above the substrate surface (figure 4.11 (c)-(d)). The shortening of the processes continued while the overall shape of the cell bodies became more spherical as pSi pore size continued to decrease (figure 4.11 (e)-(f)). On the 50-100nm region of graded pSi, cells were completely rounded and formed multilayered clusters (figure 4.11 (g)-(h)).

The first indication of the recovery of the typical neuroblastoma cell morphology and of the development of processes was observed on the 20-50 nm pore size regime (figure 4.11 (i)-(j)).

Cells growing here had the typical teardrop-shape morphology but elaborated only short, thin and branched processes. In contrast, on the 5-20 nm pore size regime, cellular processes were long and slim (figure 4.11 (k)-(l)). On all surfaces so far (even the mesoporous surface with pore sizes < 20 nm), the cell bodies appeared elevated from the substrate surface. This is in sharp contrast to the cells residing on flat silicon where the cell bodies were generally more flattened and in immediate contact with the substratum.

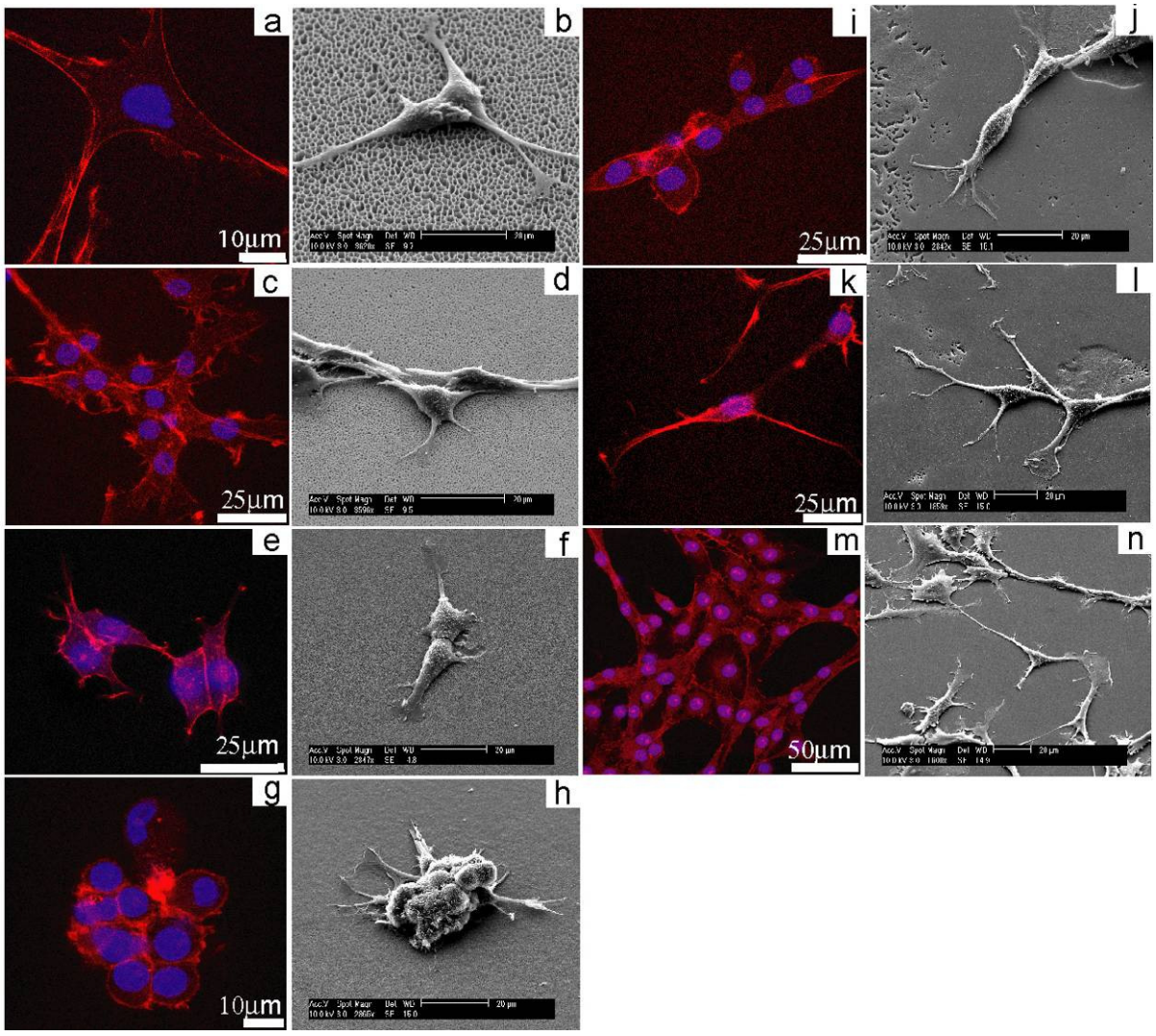

Figure 4.11 - Morphological analysis of neuroblastoma cells. Laser scanning confocal microscopy (cells stained with Hoechst 33342 and Alexa Fluor® phalloidin conjugate) after 24 hours of growth on (a) 1000-3000 nm, (c) 300-1000 nm, (e) 100-300 nm, (g) 50-100 nm, (i) 20-50 nm, (k) 5-20 nm porous silicon regions and (m) flat silicon. Corresponding SEM micrographs of cells growing on (b) 1000-3000 nm, (d) 300-1000 nm, (f) 100-300 nm, (h) 50-100 nm, (j) 20-50 nm, (l) 5-20 nm porous silicon regions and (n) flat silicon are shown on the right.

Figure 4.11 (a) also shows the presence of straight running actin bundles in the 1000-3000nm region, indicating a polarization stage of spreading[91] which in turn is suggestive of a motile morphology. Figure 4.11 (c), (e), (g) and (i) show increasing signs of circumferential actin filament clustering along the periphery of neuroblastoma cells which is a sign of cell adhesion. On the 5-20 nm pore size region (figure 4.10 (k)) intensive actin staining was observed, particularly within the neuritic processes which are indicative of cell spreading. Finally, cells growing on flat silicon stained more evenly for actin (figure 4.11 (m)).

4.2.2.4 Cell density, area and length

To gain a more quantitative understanding of cell adhesion on this surface, the density, area and length of adherent neuroblastoma cells were determined for each of the six regions of graded pSi (figure 4.12 (a)) and the results were analysed by a one-way ANOVA test.

Cell density determined from Hoechst staining was found to be highest on flat silicon (1900 cells/mm^2) consistent with the trend observed in figure 4.10. Cell density was significantly reduced (1300 cells/mm^2) on the 1000–3000 nm region of pSi ($p < 0.005$), in accordance with the results presented in figure 4.10 (a) where cells appeared to organise themselves in a honeycomb network rather than forming a confluent monolayer. Cell density decreased with decreasing pore size until a minimum in cell density was reached on the 100–300 nm region of the pSi surface. Below this pore size range, cell density increased again. The density of cells on the 5–20 nm region approached the density of cells growing on the flat silicon substrate (1600 cells/mm^2 vs. 1900 cells/mm^2). Nevertheless, the significant difference ($p < 0.005$) in cell density between flat and mesoporous silicon (pore diameter < 20 nm) suggests that surface topography, even at the nanoscale, was felt by adhering and growing cells.

Cell length and area were used as additional parameters to describe neuroblastoma cell growth on the graded pSi. Figure 4.12 (b)-(c) shows cell length and area calculated from laser scanning confocal microscopy images for the six different regions of graded pSi. The length of individual cells was determined by measuring the lengths of the longest processes from the cell and adding those to the diameter of the cell body. Cell area was found to be largest on the region of 1000–3000 nm pore size (375 μm^2) and smallest on the region of 50–100 nm pore size (120 μm^2). Notably, cells residing on the 1000–3000nm pSi covered an

area that was even larger than that occupied by cells residing on flat silicon (350 μm^2), but the difference was not statistically significant. Similarly, cells growing on the micron size pores were in average 15 μm longer than on flat silicon (70 μm vs. 55 μm). However, cell density on flat silicon was almost twice that on the graded pSi with micron size pores (figure 4.12 (a)). These results suggest that cells reacted to the large pores presented by expanding in order to adhere to the substrate surface. This finding is in agreement with the SEM results. On the neighbouring regions with 300–1000 nm and 100–300 nm pore sizes, cells were significantly shorter ($p < 0.005$), while still maintaining a spreading area comparable to that determined for flat silicon. Cell area and length reached minimum values for the smallest macroporous region of 50–100 nm pore size, while cell density was lowest on the 100–300 nm region (Figure 4.12 (a)). The reason for a higher cell density for the 50–100 nm region compared to the density on the 100–300 nm region could be attributed to the presence of clumps of multilayered cells (figure 4.11 (g)–(h)) resulting in higher cell counts compared to the surfaces with only substrate-anchored cells. For the mesoporous regions (20–50 nm and 5–20 nm), we observed an increase in cell area compared to the macroporous region of 50–100 nm. The difference between the smallest macroporous region and the largest mesoporous region was not statistically significant ($p > 0.3$). However, the difference between the 50–100 nm and the 5–20 nm regions was highly significant ($p < 0.005$). Cell area for the 20–50 nm region was about 140 μm^2, about 180 μm^2 on the 5–20 nm region and finally 350 μm^2 for flat silicon. On the other hand, moving from the 50–100 nm to the 20–50 nm region, cellular length more than doubled ($p < 0.005$). For the 5–20 nm region, another 60% increase in cell length was registered. The difference in cell length between the smallest porous region and flat silicon was not significant. The one-way ANOVA test also confirmed that the change in pore size has a significant influence ($p \leq 0.005$) in general on the three different cell parameter (density, cell density and cell area) investigated.

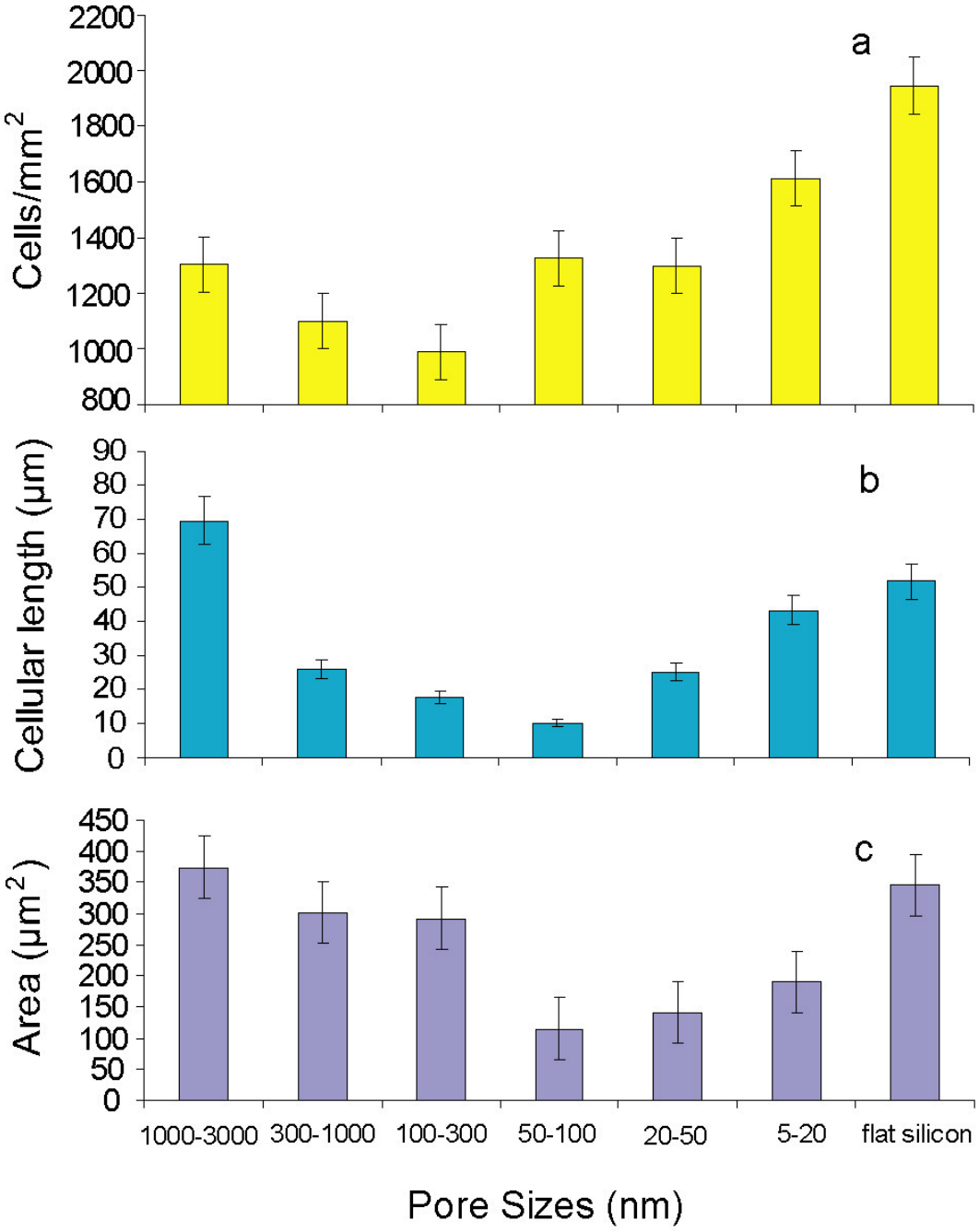

Figure 4.11 - (a) Cell density of neuroblastoma cells on six regions of graded pSi and flat silicon after 24h incubation, n=3. (b) Cellular length, n=10 and (c) cell adhesion area on graded pSi and flat silicon n=50.

4.2.2.5 Analysis of filopodia formation

Filopodia formation for cells growing on these samples could give clues to the behaviour of these cells since these cellular projections contribute to intercellular communication, cell adhesion and motility[92] and are often considered precursors of synapses in neurons[83]. We found that the length and nature of filopodia formed by neuroblastoma was affected by the pSi pore size presented to these cells. As shown in figure 4.13(a), cells adhering on the 1000-3000 nm pore size region of graded pSi do not present any notable filopodia protruding from the neuritic processes. The flattening of the lamellipodia-like processes at their motile ends (highlighted by white arrows in figure 4.13(a) suggests that those are regions where the main focal anchorage to the substrate for the entire cell occurs since the main cell body appears to be elevated from the substrate (figure 4.11(b)). Similar features were observed for cells growing on pores 100-1000 nm in diameter although the average length of the neuritic processes was much shorter. Furthermore, on the 100-300 nm region, we observed several short filopodia-like protrusions (labelled by white arrows) from the main cell body that anchors the cell to the substrate. Interestingly, these anchorage points exert sufficient pressure to break the porous film (figure 4.13(c)). Shorter and fewer protrusions between 2-4 μm were found at the base of the clustered cells of spherical phenotype on the regions between 50-100 nm as shown in figure 4.13(d). The clustering and short filopodia projections appear to imply that contact between the cell and the substratum was weak and cells are not "comfortable" residing on this topography[84]. Recovery of formation of processes and the re-initiation of filopodia outgrowth was observed in region between 20-50 nm, as shown in figure 4.13(e), suggesting that cells are able to overcome the cell spreading inhibiting substrate effect of pores > 50 nm. Subsequently, multiple thin filopodia ranging from 20-40 μm in length were found to branch out from the main neuritic processes on the mesoporous

regions (figure 4.13(f)). More numerous filopodia were observed branching from the neuritic processes of neuroblastoma cells growing on flat silicon.

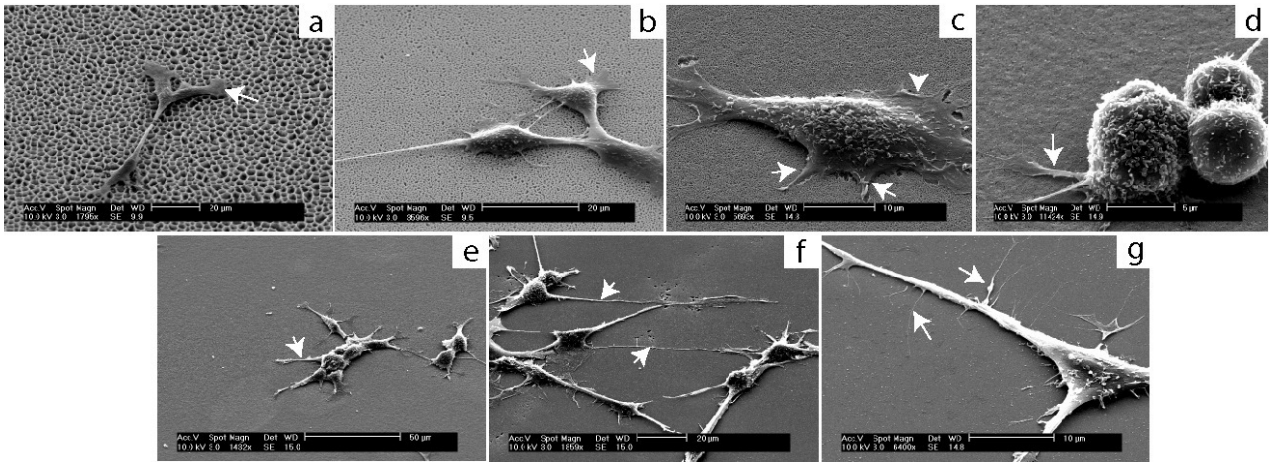

Figure 4.13 - Filopodia formation of neuroblastoma cells on the laterally graded pSi observed in SEM after 24h incubation time. (a) SEM of neuroblastoma cells on the 1000-3000 nm, arrow depicting the flattening of the lamellipodia serving as anchorage points. Filopodia were absent in this region. (b) the 300-1000 nm, arrows highlighting the flattening of the lamellipodia closer to the main cell body (c) the 100-300 nm, shorter filopodia-like protrusions between 2-4 µm as indicated by the arrows while arrowhead show the lamellipodia.(d) Spherical neuroblastoma cells adhering on the 50-100 nm pore size region with relatively short and thick filopodia at the base. (e) 20-50 nm, initial recovery of the formation of neuritic processes as indicated by the arrow. (f) 5-20 nm, processes were long, spanning up to 40 µm from the cell body with significant outgrowth of filopodia as denoted by the arrows. (g) A neuroblastoma cell growing on the flat silicon surface. Arrows indicate filopodia from a main neuritic process.

We have also established a general trend between cell adhesion and spreading. At regions between 1000-3000 nm, pore sizes were too large for filopodia to find anchorage points on the substrate. This explains the absence of filopodia-like protrusions in figure 4.11(a). Cells growing on this region were notably elevated above the substrate (figure 4.11(b)). The only attachment points for cells growing on this pore size regime are the lamellipodia at the ends of the cellular processes. Furthermore, in response to this topography, neuroblastoma cells were observed to have increased in volume and elaborated long processes to gain sufficient support from cell-cell contacts rather than relying on cell-substratum contact[93].

As the size of the pores decreases from 100 nm to 1000 nm, an increased incidence of thin protrusions from the cell body was noticed. At the same time, the main processes became shorter. The process termini were flattened out onto the substrate surface, similar to the effect seen on the 1000-3000 nm region.

On the 50-100 nm region, cell clustering was observed. Cells had a distinct spherical morphology. Filopodia-like projections to the surface were observed arising from the base of the cell clusters. A gradual recovery of the typical neuroblastoma cell morphology occurred for neuroblastoma growing on mesoporous (< 50 nm pore diameter) pSi.

Several important observations can be made from growing neurons on an asymmetrically anodised pSi surface. Firstly, the cell bodies adhering to pSi films were slightly raised above the substrate surface in contrast to cells cultured on flat silicon. Similar observations were made in earlier studies on cellular adhesion on rough surfaces[94]. The cell's main body hence resists attachment and flattening on a porous substrate even with mesoporous (< 50 nm) pore sizes.

4.2.3 Conclusions

There has been extensive research carried out on the induction of neuritogenesis of neuroblastoma cells[95-98]. However, it is not our intention here to study the mechanism of processes propagation, but rather to examine the effects on neuronal cell adhesion and spreading when grown for short culture periods on laterally graded pSi films.

Engineering platforms for tissue culture and engineering and evaluation of growth on 3-dimensional surfaces can be a difficult and time-consuming process. Topography and in particular porosity are key determinants of cellular morphology. Such morphological differences might result in a range of differing metabolism and functionality. We have used continuous porous silicon gradients to establish the effects of substrate pore size on cell viability and morphology. We propose that such topographically graded surfaces have the potential to significantly reduce the numbers of samples and the analysis time required in the investigation of cell surface interactions in comparison with the conventional one data point-one sample analysis. Using neuroblastoma cells, we observed cells to display morphological characteristics that are influenced by their ability to adhere on the surface. On the large pores (1000-3000 nm), cells were not able to adhere optimally on surfaces, but could stabilise themselves through cell-cell contacts, reducing the need for cell-substratum contact. We have found that between 50-100nm, cells adhere poorly on the surface. This may prove to be very useful to designing low-fouling biomaterials in conjunction with chemical surface treatments to direct neuritic growth[99]. By comparison with flat silicon, our results show that even mesoporosity of < 20 nm exerts an influence on neuroblastoma growth.

4.3 Multidirectional photonic mirror gradients

The use of photonic materials and devices has gained significant interest in recent years, in particular in the area of information technology[100-103]. These extensive explorations into photonic materials are strongly motivated by the fact that photons can move faster than electrons and thus carry far more information than conventional electronic circuits per unit time[100,101]. Furthermore, whilst the design of electronic circuits is inevitably limited by the fundamentals of device miniaturisation and unavoidable information loss, a photonic crystal based optical chip will, in principle, be unbound by these restrictions[100]. Ideally, such an optical chip must possess certain distinctive optical properties such as inhibition of spontaneous emission and low-loss waveguiding. These properties can be easily realised on 1D photonic crystals made from porous composites, which have been illustrated as excellent platforms for tailoring low-loss photonic bandgaps[104,105]. Comprised of periodically differing dielectric layers with well-ordered lattice spacings, these multilayered materials can control and manipulate electromagnetic wave propagations in a similar manner to the way semiconductor chips direct the electron movement by defining energy bands[105]. Photonic crystals show a high level of confinement and guidance of photons which is of prime importance in the quest for true photonic integrated circuit[102,106].

The use of porous silicon (pSi) for the construction of photonic mirrors is well documented[5, 27,107-120]. The pore dimensions of pSi span the nanoscale and range from a few nanometers to micrometers[2,121]. pSi surfaces also show other interesting optical features such as photoluminescence[122]. The surface chemistry of pSi can be easily controlled using hydrosilylation, oxidisation or oxidation followed by silanisation to introduce the desired

surface chemistry[99,123]. In addition, due to its biocompatibility, pSi is frequently employed for a wide range of biological investigations[2,31,99].

Porous materials have a different refractive index compared to bulk material and if the pore sizes are much smaller than the wavelengths of the incident electromagnetic field, the porous layer will assume an effective dielectric function. The overall dielectric effectiveness is dependent on the ratio of the dielectric functions from both the bulk material and the medium within the pores. In the case of pSi, this ratio can be effectively tuned by controlling the anodisation current during the fabrication process. pSi-based photonic mirrors or filters have been fabricated by oscillating the anodisation current which produces periodic dielectric constant variations along the optical axis[110,111,114,119]. If the transition between the high and low anodisation currents is abrupt, a multilayered profile will have distinctively spaced lattices of low and high refractive indices, respectively. Such conventional step-index mirrors are termed distributed Bragg reflectors[124-127]. However, in the case of a sinusoidal modulation of current, there will be gradual sinusoidal variation in refractive index and the resulting materials are termed rugate mirrors[27,111,114,119]. Due to the smooth refractive index variation found in rugate mirrors, optical features such as bandgap confinement and harmonics are often improved with respect to Bragg reflectors[111,114]. Recent studies have suggested a trend in preference of the pSi-based rugate profile over Bragg reflectors as platforms for manipulating electromagnetic waves and such mirrors have already found applications as optical chemo- and biosensors[111,128].

In the past, evaporation and plasma deposition had been successfully utilised to produce rugates mirrors, however these deposition techniques prove to be time-consuming and expensive[3,129]. The major advantage of electrochemical anodisation of pSi over these

methods is that a rugate profile can be easily and quickly (within a few minutes) fashioned by simply introducing a sinusoidal current during the anodisation process. As a extension to this technique, the Sailor group has recently described a method for producing a laterally graded rugate mirror by asymmetrically anodising the pSi surface[27]. In a setup similar to the one depicted in figure 4.14 (a)-(b), the potential at the surface/electrolyte interface varies as a function of distance from the platinum electrode due to resistivity from the electrolyte solution. This leads to a reduction in current density as the distance from the counter electrode increases and the resulting surface displays a lateral gradient of porosity (figure 4.14 (c). Such laterally graded pSi has been employed for sizing of proteins and for the investigation of cell surface interactions[1,2]. By further applying a square-wave or sinusoidal anodising current during asymmetric anodisation, the pSi surface will assume a Bragg or rugate profile, respectively. The resulting material is of rainbow-like appearance with laterally graded reflectance bands (photonic stop-bands) across the surface[27].

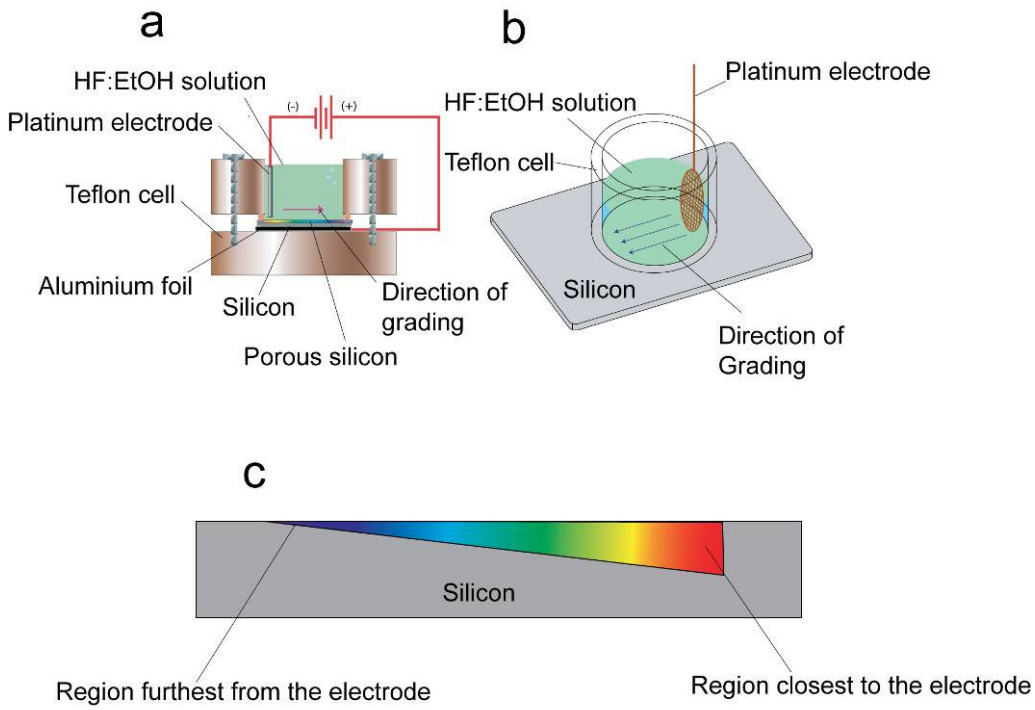

Figure 4.14. Schematic of the asymmetric anodisation setup to produce laterally graded pSi. (a) Cross-sectional view and (b) 3D view of cell. Note that the direction of the photonic gradient is perpendicular to the face of the electrode. Due to the reduction in anodisation current experienced by the surface as it progresses further from the electrode, the film thickness will decrease with increasing distance from the electrode in (c).

Asymmetric anodisation of silicon is an inexpensive method to fabricate a large range of reflectance peaks on a single material. Such lateral photonic mirror gradients have been used as gradient refractive index devices in integrated optical circuits and solar cell anti-reflection applications[130-132]. The most obvious advantage of using a pSi-based photonic gradient is certainly its compatibility with silicon optoelectronics. The additional feature of pSi mirror gradients that would distinguish them from other photonic gradients is that multidirectional photonic mirror gradients can potentially be integrated within a single substrate. Thus, in this paper, such multidirectional stacked pSi-based photonic mirror gradients with Bragg and rugate profiles were fabricated and characterised by optical reflectivity measurements and SEM. These multidirectional photonic films were also liberated from the bulk silicon and embedded in polydimethylsiloxane (PDMS) to form a foldable photonic material.

4.3.1 Methods and Materials

4.3.1.1 Anodisation procedure

All pSi samples were prepared from p-type (boron-doped) silicon wafers with <100> orientation and resistivity of 0.0005-0.001 Ω.cm (Virginia Semiconductors). Anodisation was performed in a Teflon etching cell using a 3:1 (v/v) solution of 49 % aqueous HF/EtOH by placing an a circular Pt mesh electrode at a height of approximately 2 mm above the silicon surface, with the electrode oriented parallel to the surface normal. All pSi surfaces had a diameter of approximately 1.5 cm and a surface area in the order of 1.77 cm^2.

4.3.1.2 Single photonic gradient

For fabricating a monodirectional rugate gradient, a sinusoidal current waveform oscillating from 40 mA to 80 mA with 70 repeats and a periodicity of 10 s was applied to the surface. Monodirectional Bragg gradients were produced by applying a square-wave current between 40 mA and 80 mA with 70 repeats and a periodicity of 10s. After the anodisation, the electrolyte solution was removed from the etching well and the samples were rinsed with methanol, acetone and dichloromethane and dried under a stream of N_2 gas. Ten optical reflectivity measurements were taken at 1 mm interval across each gradient surface starting from the region that was closest to the Pt mesh electrode during etching and scanning along the direction that is perpendicular to where the face of the Pt mesh electrode had been positioned (see figure 4.14 (b)).

4.3.1.3 Bidirectional rugate gradients

Bidirectional rugate gradients were fabricated by asymmetrically anodisation with a sinusoidal current waveform oscillating between 40 mA to 80 mA with 30 repeats and a periodicity of 10s. Anodisation was stopped and the Pt electrode was manually re-positioned at the opposite end of the silicon sample and an identical anodisation run was performed for another 30 periods. In addition, a 90° bidirectional gradient was also fabricated asymmetrically anodising from one end of the silicon surface with a sinusoidal current waveform oscillating between 40 mA to 80 mA with 30 repeats and a periodicity of 10s and subsequent re-positioning of the electrode at 90° relative to its first position. The second gradient was asymmetrically anodised with a sinusoidal current waveform oscillating from 80 mA to 120 mA with 10s periodicity for 30 repeats. After anodisation, the electrolyte solution was removed from the etching well and the samples were rinsed with methanol, acetone and dichloromethane and dried under a stream of N_2 gas. Five reflectance measurements were taken at 2 mm intervals each across each gradient surface starting from the region that was closest to the Pt mesh electrode during etching and gradually moving along the direction that was perpendicular to where the face of the Pt mesh electrode had been positioned.

4.3.1.4 Tridirectional rugate gradients

Tridirectional rugate gradients were fabricated by asymmetrically anodising from one end of the silicon surface with a sinusoidal current waveform oscillating from 40 mA to 80 mA with 20 repeats and a periodicity of 10s. Anodisation was stopped and the platinum electrode was manually repositioned at the periphery of silicon surface at approximately 120° clockwise relative to its initial position and the identical anodisation run was performed for another 20

periods. After the second anodisation, the Pt electrode was manually repositioned for the third time at approximately 120° clockwise relative to the second position and a third anodisation run was performed for a further 20 periods. At the end of the anodisation, the electrolyte solution was removed from the etching well and the surface was rinsed with methanol, acetone and dichloromethane and dried under a stream of N_2 gas.

4.3.1.5 Freestanding photonic gradients

Immediately upon the fabrication of the photonic gradients on the silicon support, a mechanical support layer beneath the optical gradients was incorporated by anodising the surface with a mesh electrode parallel to the silicon surface at 100 mA in 3:1 HF/EtOH for 30 mins. Freestanding photonic gradients were obtained by applying an electropolishing current of 450 mA in 1:1 HF/EtOH for 1 min. The electrolyte solution was then removed from the etching well and these films were then rinsed with EtOH and were allowed to dry at room temperature. The photonic films were gently placed onto a slab of pre-cured PDMS (Sylgard 184), covered with a second layer of liquid PDMS and finally cured in the oven at 120ºC for an hour.

4.3.1.6 Optical reflectivity measurements

Optical reflectivity spectra from pSi surfaces were obtained using an Ocean Optics S2000 detector operating in the range of 300-1000 nm and a tungsten light source. Samples were illuminated through a bifurcated optical fibre with collimating lens which focused the light to a 500 μm diameter spot. Illumination and detection of the reflected light was done at an incident angle of 0° to the surface normal.

4.3.1.7 SEM analysis

SEM was performed on a Philips XL30 field emission scanning electron microscope with an acceleration voltage of 10 kV and a capture angle of 90˚ to observe the cross-section of the multiple photonic gradients.

4.3.2 Results and Discussion

4.3.2.1 Single Rugate and Bragg mirror gradients

In order to generate periodic layers of alternating high and low refractive indices, we periodically modulated the anodising current between 40 and 80 mA over 70 periods. We used square-wave and sinusoidal current modulation to produce Bragg reflectors and rugate filters, respectively.

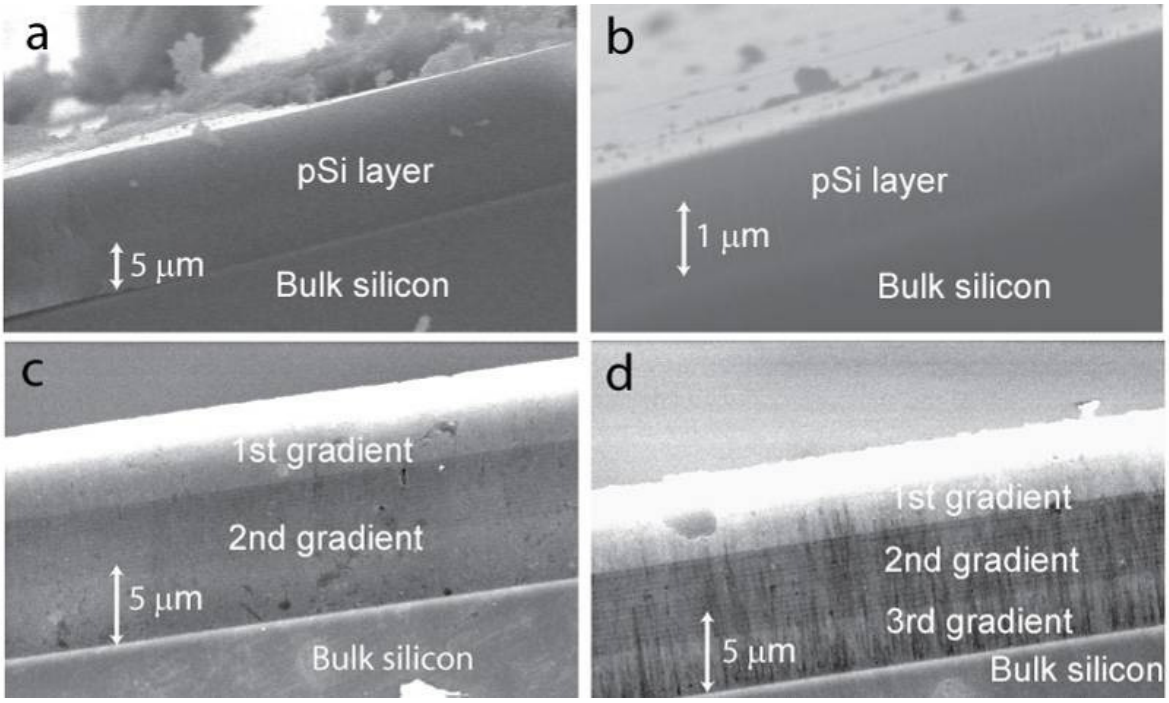

Figure 4.15. SEM cross-section of a single rugate gradient (70 periods) at (a) closest to the electrode where the thickness is 15 μm and (b) at region furthest from the electrode where the thickness is 1.7 μm. The thickness of the film decreases with increasing distance from the electrode. SEM cross-section of (c) a bidirectional 180º gradient (30 periods per gradient layer, a total of 60 periods) and (d) a tridirectional 120º gradient (20 periods per gradient layer for a total of 60 periods).

Due to the lateral gradient of current density during anodisation, we expected a decrease in gradient layer thickness with increasing distance from the electrode source (as depicted in figure 4.14 (c)). This thinning of the mirror layer was confirmed by SEM as shown in figure

4.15 (a)-(d). SEM analysis shows that the thickness of the layer ranged from 1.7 µm at a position 10 mm away from the electrode source to 15µm at the region closest to the electrode (position 0 mm). Similar wedge-shaped pSi layers were reported by Bohn et al.[133].

Photographs of rugate and Bragg gradients produced by this technique are shown in Figure 4.16 (a) and (c) and the respective optical reflectivity spectra are presented in figure 4.16 (b) and d (reflectance spectra were acquired every mm over a 10 mm region). Figure 4.16 (a) shows that asymmetrical anodisation alternating between two current densities using a sinusoidal current profile affords rugate gradients with a smooth colour transition from red close to the region of highest etching current to blue in the region which experienced the lowest etching current. Figure 4.16 (c) displays a Bragg gradient with clearly visible reflectance bands on the surface. The structural colour shift across the surface was not as smooth as compared to the rugate gradient.

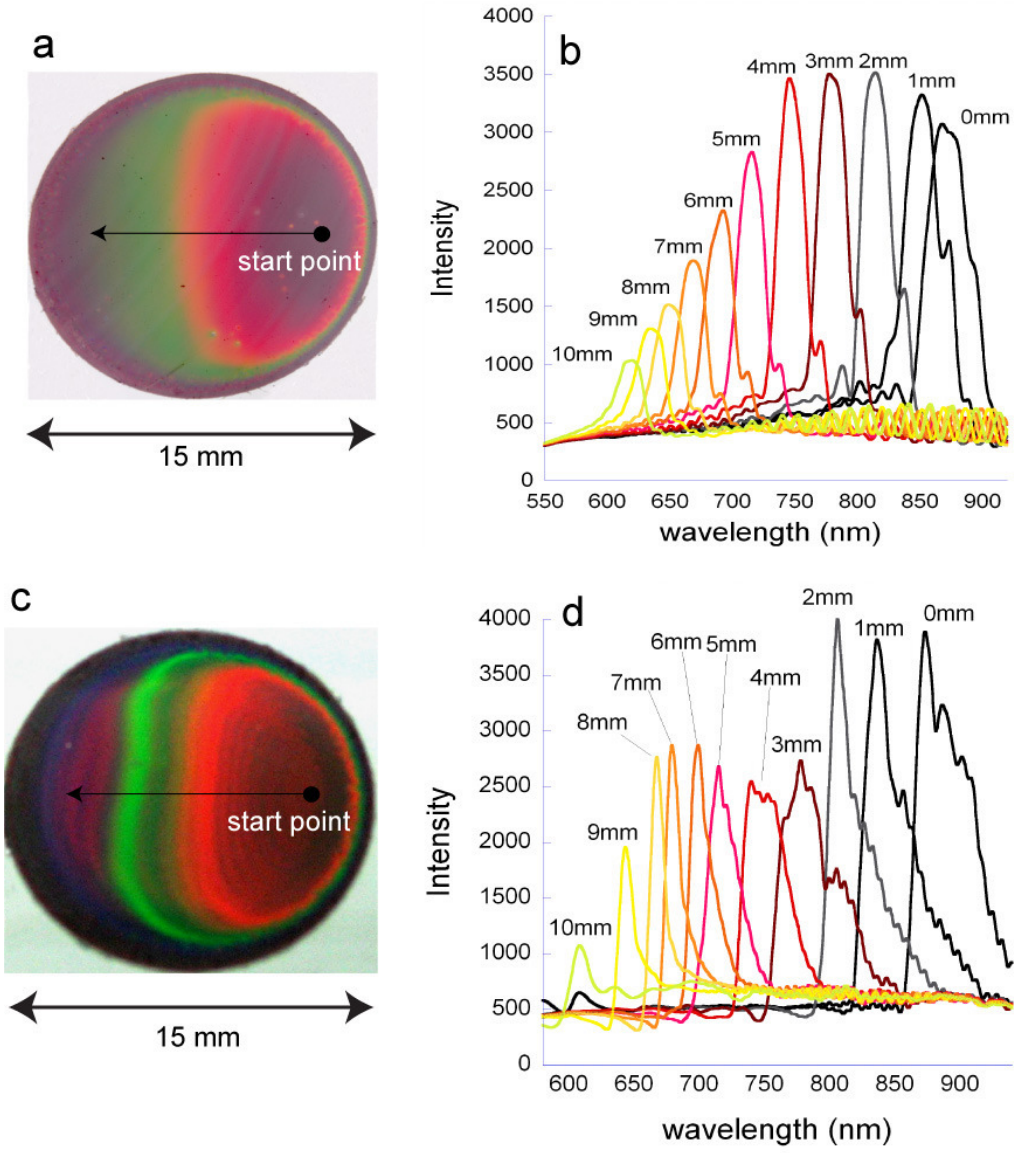

Figure 4.16. (a) Photograph of the surface for a rugate gradient, which shows a smooth transition in structural colour across the surface. (b) The measured reflectance spectra are as shown for rugate gradient. (c) Bragg gradient displaying a surface with structural colour bands and (d) the measured reflectance spectra for the Bragg gradient. Reflectance spectra were taken every mm over 10 mm starting from the middle of the region closest to the electrode and moving across the pSi surface in a direction parallel to the direction of the grading (as indicated by the arrow).

Contrary to the visual observations and the photographic representation, which show reflectance colours ranging from red to blue, the reflectance spectra display reflectance bands corresponding to photonic bandgaps ranging from 900 nm (NIR) at the region closest to the electrode to 600 nm (orange) at the region furthest away from the electrode. We attribute the

discrepancy between the observed spectral features and the photographic representation discrepancy to a broad background reflectance which contributes to the structural colour observed by the camera and the naked eye.

The reflectance peak position blue-shifted around 25 nm for every mm distance from the electrode region. The blue shift is attributed to the reduction of pore size and porosity with increasing distance to the electrode. Upon further inspection, the reflectance spectra showed asymmetrical band shapes, tailing on the long wavelength side of the peak and multiple satellite bands up to 5-6 mm away from the electrode. In contrast to the rugate gradient, the reflectance bands on the Bragg gradient became sharper towards lower wavelengths.

We also observed for both the Bragg and the rugate gradients a reduction of peak intensity for spectra acquired in regions further away from the position of the electrode during anodisation. This can be attributed to the thinning of the multilayer stack, reducing the effectiveness of the photonic mirror.

To further characterise the photonic gradients produced, an analysis of the full-width at half maximum (FWHM) rugate reflector stop-bands was performed along the direction of the gradient. The optical value of light confinement within the gradient, the quality factor (Q), as defined by the resonance wavelength divided by the FWHM, was also determined[134]. As illustrated in figure 4.17 (a), the FWHM (28-31 nm) and the Q factor (20-28 nm) were more consistent across the rugate gradient compared to the Bragg gradient. More than 6 mm from the position of the electrode, the Bragg gradient shows improved optical confinement compared to the rugate gradient (figure 4.17 (b)). Notably, our anodisation procedure produced superior photonic gradients in terms of light confinement and range of reflected

colours compared to the ones reported in the literature so far with FWHM of around 100 nm[135]. However, the FWHM of the reflectance bands in the rugate gradient is significantly higher than in conventional rugate mirrors[136].

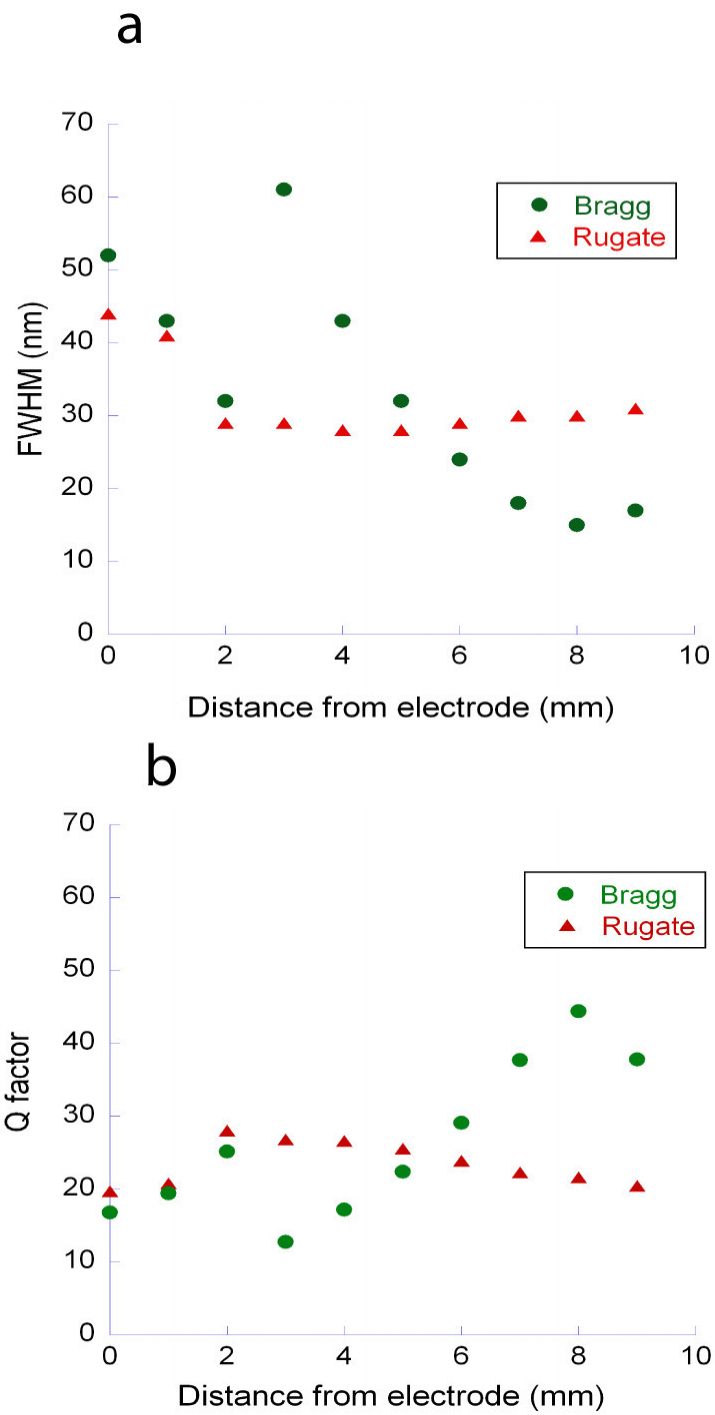

Figure 4.17 (a) FWHM and (b) Q factor analysis for single Bragg and rugate gradients of 70 periods.

4.3.2.2 Bidirectional Rugate gradients

Since the rugate gradient gave more consistent photonic properties, we decided to utilise this rugate profiles for the production of bidirectional pSi photonic mirror gradients by two subsequent asymmetric anodisations, changing the electrode position after the first anodisation. This resulted in two overlayed gradients with different directional vectors.

We conjectured that upon fabrication of two gradients in opposing directions, the photonic mirror should display two distinct reflectance bands on the periphery of the sample, one from each gradient, which should converge in its centre. Figure 4.18 (a) shows reflectance spectra taken of two overlayed rugate gradients anodised at 180° relative to each other while figure 4.18 (b) shows a photograph of this surface. Measurements were taken at 2 mm intervals from the position of the electrode for the lower gradient (position 0 mm), moving in a direction towards the position of the electrode during etching of the lower gradient. The reflectance bands from the two gradient layers indeed converged roughly in the center of the sample. Both gradients covered a similar reflectance range, from 500 nm to 800 nm, but the reflectance bands from the lower gradient were somewhat attenuated, particularly at the region furthest away from the electrode during anodisation of the lower gradient (position 10 mm), which afforded reflectances peaking in the green. This was attributed the reduced thickness of the lower gradient in that region which was confirmed by SEM. The region closest to the electrode during fabrication of the lower gradient showed a thicker lower gradient layer (figure 4.15 (c)). In the SEM cross-section, two distinctive gradients can be distinguished. The thickness of the upper and lower gradient was measured at 5 µm and 9 µm, respectively. Porosity variations cannot be discerned in the upper gradient. In the lower gradient on the other hand, distinctive periods of porosity are resolved.

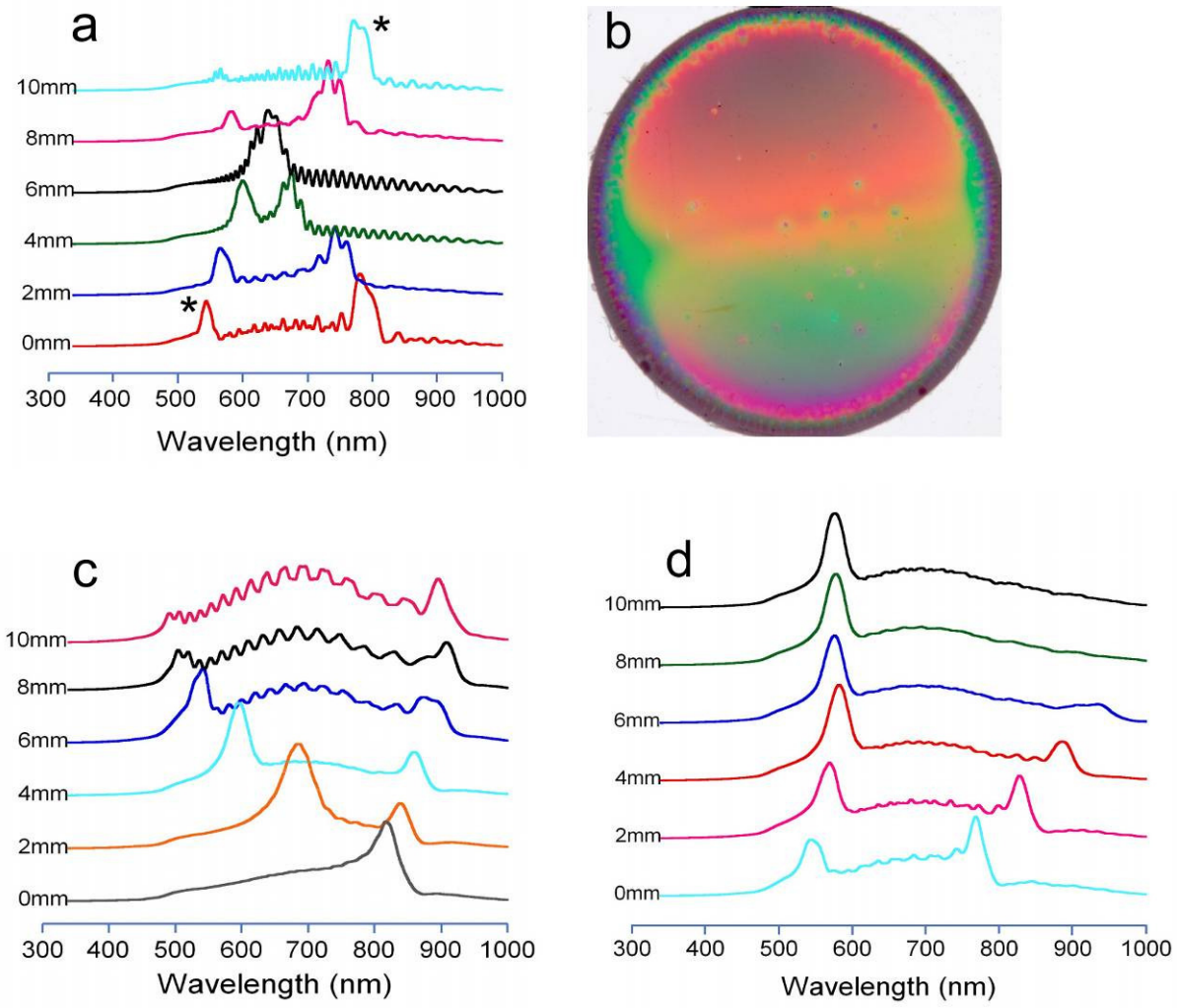

Figure 4.18. Bidirectional rugate gradients. (a) 2 x 30-period rugate gradient anodised at 180º relative to each other. The asterisk labels the stop-band from the top gradient. (b) Photograph of the bidirectional 180º rugate gradient. (c) A series of reflectance spectra from a 90º bidirectional gradient (position 0 mm = position of the electrode during anodisation of the upper gradient). (d) A series of reflectance spectra from the 90º bidirectional gradient following the direction of the lower gradient (position 0 mm = position of the electrode during anodisation of the lower gradient).

Nevertheless, our results demonstrate that two rugate gradients can be overlayed without completely masking the photonic responses from the lower gradient. Each layer was produced from 30 periods of current modulation. An increase in the number of periods resulted in thicker gradients with better light confinement, but with the disadvantage that the photonic response of the lower gradient was masked.

We further produced a perpendicular bidirectional mirror gradients (figure 4.18 (c)-(d)). Acquiring reflectance spectra in the direction of either one of the gradients should produce two reflectance bands, one roving and one relatively stable. For the upper gradient, a waveform oscillating from 40 mA to 80 mA was used, whilst the lower gradient was asymmetrically anodised with a sinusoidal current waveform oscillating from 80 mA to 120 mA. We expected these latter conditions to produce a red shift in the reflectance bands compared to the upper gradient. As shown in figure 4.18 (c), there was a shift in the rejection band from the upper gradient ranging from 820 nm to 510 nm when scanning across the surface in the direction parallel to the upper gradient. In contrast, the photonic signal from the lower gradient only shifted from 910 to 820 nm. The slight shift in the reflectance from the lower gradient is not surprising when considering that the current distribution during the asymmetric anodisation drops off from the Pt mesh electrode following a concentric arc pattern. When scanning along the direction of the lower gradient (figure 4.18 (d)), one band exhibited a minor change in the peak position between 550 nm to 590 nm (from the upper gradient), whilst reflectance bands from the lower gradient ranged from 930 nm to 760 nm. The responses from the thinner regions of the lower gradient (positions > 6 mm) were masked by the top gradient.

4.3.2.3 Tridirectional Rugate gradients

Tridirectional rugate gradients were prepared by overlaying three mirror gradients with different directional vectors. Here, the electrode was moved clockwise 120˚ along the periphery of the sample after the first and second gradient layer was produced. Figure 4.19 (a) shows a photograph of tridirectional rugate gradients. Each gradient was anodised for 20 periods with the position of the electrode highlighted in the fig. by asterisks. A series of reflectance spectra from this tridirectional gradient is shown in figure 4.19 (b)-(c).

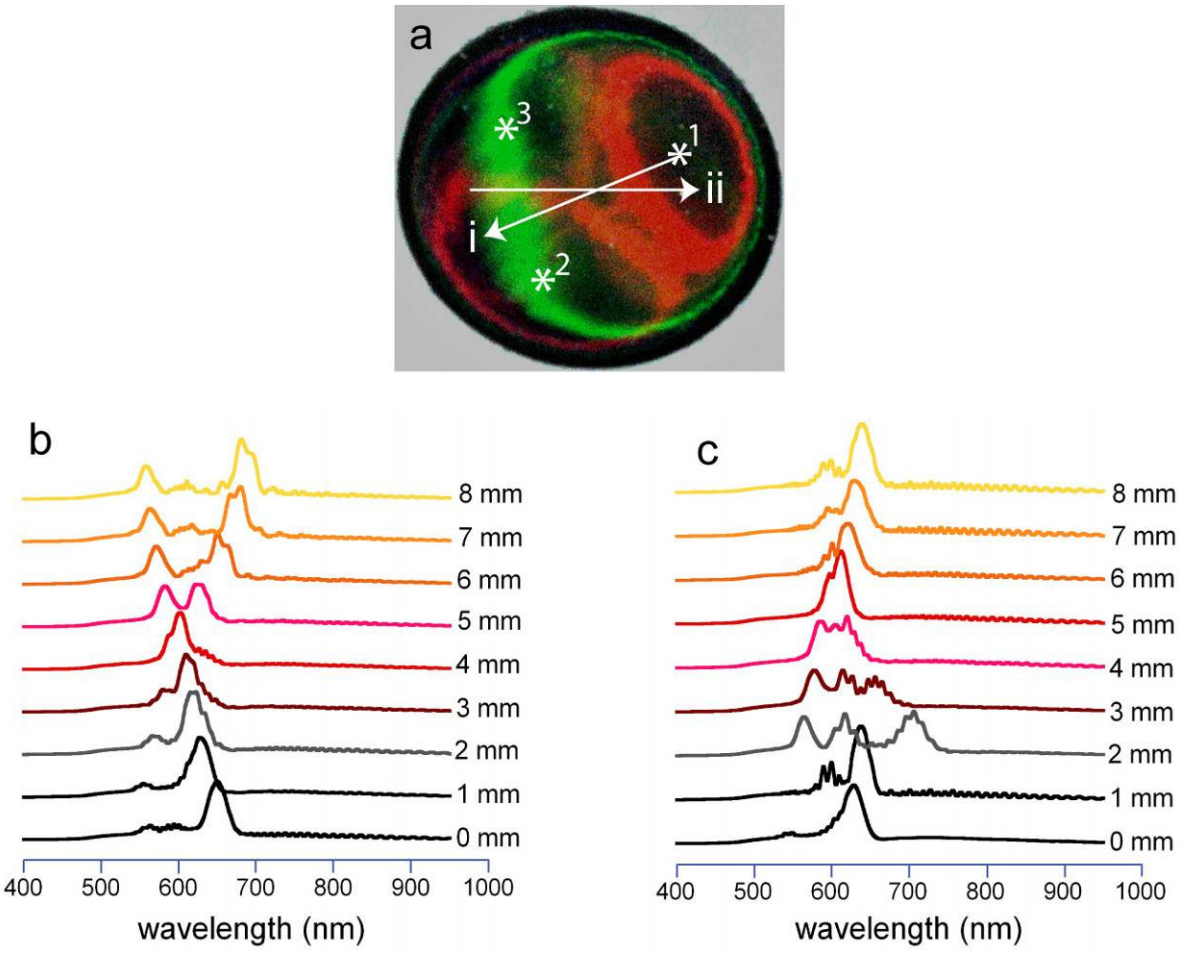

Figure 4.19. Tridirectional mirrors gradients. (a) Photograph of the tridirectional gradient. The asterisks represent the regions nearest to the electrode for the top gradient (1), the central gradient (2) and the lower gradient (3). (b) A series of reflectance spectra following the top gradient as marked i in (a). (c) A series of reflectance spectra following direction (ii).

Figure 4.19 (b) shows the reflectance spectra following the top gradient as marked **i** in the photograph (see figure 4.19 (a)). At the position 0 mm (correlating to the region closest to the electrode during anodisation), we observed a single band at 650 nm. Reflectance bands from the central and lower gradient were not observed at this position and this is presumably because they were masked by the thick top gradient. At position 2 mm, a small spectral feature was observed centered at 568 nm which is attributed to the central gradient. At position 3-4 mm, the reflectance bands converged, producing a single feature centered at 605 nm. At position 5mm, the reflectance patterns diverges to form two separate reflectance bands at 625 nm and 590 nm. We attributed the band at 625 nm and 590 nm to the central and top gradient, respectively. Subsequently, from position 6-8 nm, the two respective bands shifted further apart and finally settling at 555 nm (top gradient) and 680 (central gradient). And at 7-8 mm, the weak reflectance bands from the lower gradient at 610-615 nm could also be observed in between the two stop-bands from the upper gradients.

Figure 4.19 (c) shows a series of reflectance spectra following the direction marked **ii** in the photograph (see figure 4.19 (a)). At the position 0 mm (at the start of the arrow in the photograph), we observed a single predominant band at 630 nm with a smaller spectral feature at 545 nm. At position 2 mm, three bands were observed, each representing a stop-band from one individual gradient. These three peaks subsequently converged between 4-6 mm from the electrode, producing a single broad band centered at 615 nm. At position 8 mm, the reflectance pattern diverges to form two separate reflectance bands centered at 640 and 600 nm, respectively. The spectral feature at 640 nm was attributed to the upper gradient while the reflectance at 600 nm was assigned to the central gradient. Reflectance peaks from the lower gradient were not observed at this position and this was presumably because they were masked by the upper gradients.

SEM images of a cross-section of the tridirectional gradients were also acquired. The overall thickness of the gradient film, as shown in Figure 4.15 (d) was maintained at 14 μm, similar to the bidirectional gradients having the same number of periods (60). This SEM cross-section (figure 4.15 (d)) was obtained at a position close to the region of highest current for the central gradient. The three gradients could be clearly distinguished. The individual periods could only be resolved within the central gradient, which, as expected for this location, was considerably thicker than the other two gradients.

Here, we have overlayed three rugate gradients onto a single silicon substrate and were able to detect photonic signals from each gradient. The structures fabricated here show unique reflectance characteristics which might find applications as photonic barcodes, sensors and in micro-opto-electromechanical systems (MOEMS)[137-139].

4.3 2.4 Freestanding and PDMS-embedded photonic mirror gradients

The photonic structures generated above are still attached to the silicon wafer from which they have been generated. By applying an electropolishing current after the gradient fabrication, we were able to lift off the gradient layer(s) from the silicon to form free-standing films. Since these films fractured easily, we increased the mechanical stability of the free-standing films by anodising a mechanical support layer underneath the gradient layer. The thickened photonic film was subsequently released from the bulk silicon using electropolishing. This step produced a robust free-standing rugate gradient which could be manipulated, but fractured when attempts were made to bend the film slightly. Embedding of these films in PDMS (figure 4.20 (a), a PDMS embedded 180˚ bidirectional gradient) allowed the folding of the film (figure 4.20 (b)) without compromising structural integrity.

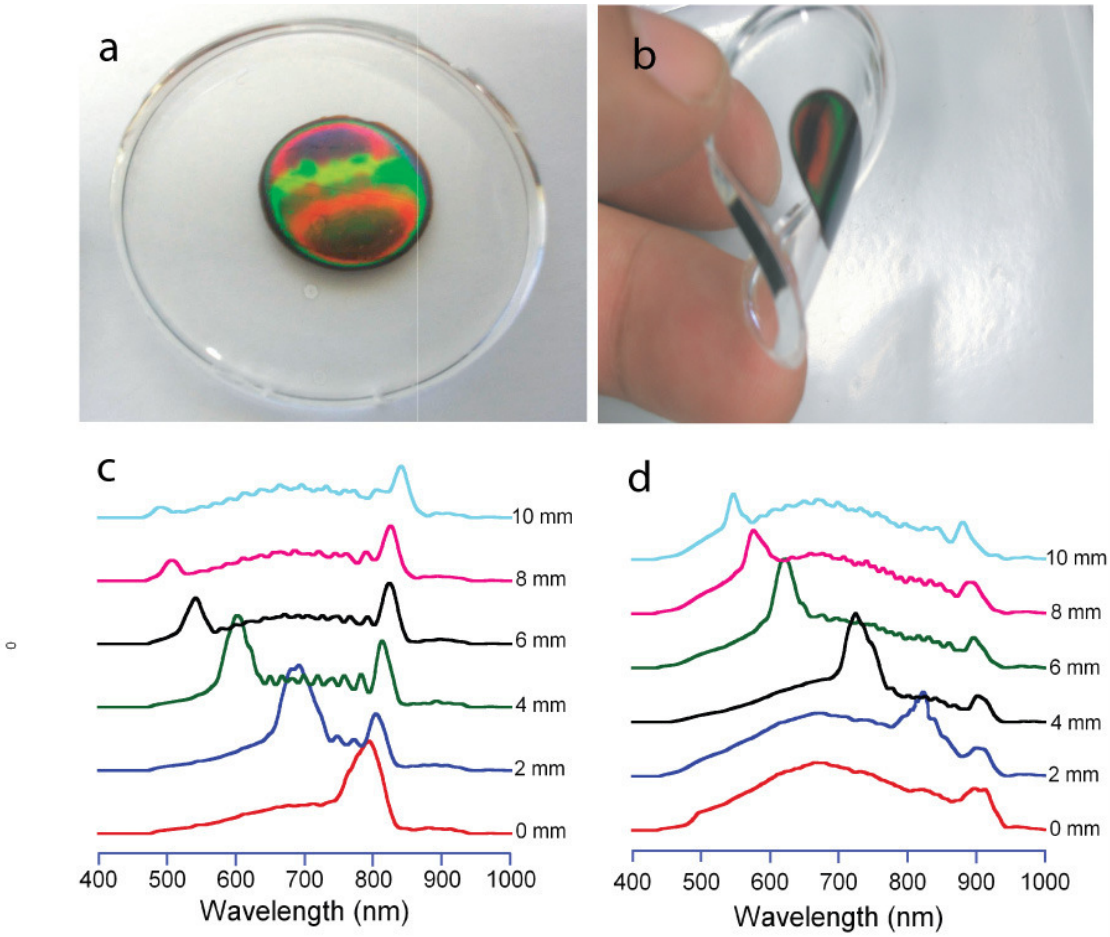

Figure 4.20. Bidirectional mirror gradients liberated from silicon substrate and embedded in PDMS. (a) Photograph of a 180° bidirectional photonic mirror gradient embedded in PDMS. (b) Photograph demonstrating that bidirectional photonic mirrors are foldable. (c) A reflectance spectra from a free-standing 90° bidirectional photonic mirror gradient before PDMS embedding and (d) after PDMS embedding.

To evaluate the reflectance pattern of a perpendicular bidirectional gradient before and after PDMS embedding, reflectance spectra were taken from the start of the top gradient before embedding in PDMS. As expected, we observed two reflectance bands, one from each gradient of the freestanding film (figure 4.20 (c)). A stable reflectance band at 820 nm corresponding to the response of the lower gradient was observed at both positions, while photonic features from the top gradient shifted from 490 nm to 790 nm. After embedding the gradient into PDMS, all reflectance bands red-shifted by approximately 55-110 nm (figure 4.20 (d)). This is due to the refractive index increase of the porous layer upon embedding in

PDMS (refractive index 1.42). However, the pattern of the reflectance shift across the surface was not affected.

4.3.3. Conclusions

Here, we have reported the fabrication of photonic mirror gradients on a silicon surface by asymmetric anodisation with an oscillating current. Optical reflectivity spectra for rugate- and Bragg-type gradients were evaluated. The rugate profile resulted in smooth gradients with reflectance bands of a consistent FHWM of ~28-31 nm. The Bragg profile on the other hand gave a more banded response along with a greater variation in photonic band characteristics such as FHWM and Q-factor. The reflectance peaks ranged from 900-600 nm for both rugate and Bragg gradients with 70 periods.

We then overlayed several photonic mirror gradients with different directional vectors on a silicon substrate and obtained optical reflectivity spectra across the sample. We were able to observe spectral features relating to photonic stop-bands from up to three gradients. However, a gradient thickness of below 10 μm is required to prevent masking of the signal from lower gradients. Finally, we prepared free-standing multidirectional rugate gradients by adding a mechanical support layer beneath the photonic layers. The free-standing films were subsequently embedded in PDMS and retained their unique reflectance patterns. The embedded films could be easily handled and even folded repeatedly without film fracture. Whilst we have tuned the rejection bands to be mainly within the visible spectrum, it is possible to fabricate mirror gradients with different reflectance ranges.

The approach presented here results in photonic gradient structures with position-dependent spectral information, which are inexpensive to produce and compatible with silicon based optoelectronics. We believe that these photonic mirror gradients can easily find applications

in gradient refractive index devices, MOEMS, photonic barcodes and also as chemical sensors

References

1. Collins, B. E.; Dancil, K. P. S.; Abbi, G.; Sailor, M. J., Determining protein size using an electrochemically machined pore gradient in silicon. ***Advanced Functional Materials*** **2002, 12, (3), 187-191.**

2. Khung, Y. L.; Barritt, G.; Voelcker, N. H., Using continuous porous silicon gradients to study the influence of surface topography on the behaviour of neuroblastoma cells. ***Experimental Cell Research*** **2008, 314, (4), 789-800.**

3. Bartzsch, H.; Lange, S.; Frach, R.; Goedicke, K., Graded refractive index layer systems for antireflective coatings and rugate filters deposited by reactive pulse magnetron sputtering. ***Surface & Coatings Technology*** **2004, 180-81, 616-620.**

4. Babchenko, A.; Maryles, J., Graded-index plastic optical fiber for deformation sensing. ***Optics And Lasers In Engineering*** **2007, 45, (7), 757-760.**

5. Alvarez, S. D.; Schwartz, M. P.; Migliori, B.; Rang, C. U.; Chao, L.; Sailor, M. J., Using a porous silicon photonic crystal for bacterial cell-based biosensing. ***Physica Status Solidi a-Applications and Materials Science*** **2007, 204, (5), 1439-1443.**

6. Blossey, R., Self-cleaning surfaces - virtual realities. ***Nature Materials*** **2003, 2, (5), 301-306.**

7. Onda, T.; Shibuichi, S.; Satoh, N.; Tsujii, K., Super-Water-Repellent Fractal Surfaces. ***Langmuir*** **1996, 12, (9), 2125-7.**

8. Geoghegan, M.; Krausch, G., Wetting at polymer surfaces and interfaces. ***Progress in Polymer Science*** **2002, 28, (2), 261-302.**

9. Khang, G.; Hyeong, J.; Cho, J. C.; Rhee, J. M.; Lee, H. B., Improvement of wetting property for porous PLGA scaffold by physicochemical treatment. ***Polymer (Korea)*** **1999, 23, (6), 861-868.**

10. Lussi, J. W.; Michel, R.; Reviakine, I.; Falconnet, D.; Goessl, A.; Csucs, G.; Hubbell, J. A.; Textor, M., A novel generic platform for chemical patterning of surfaces. ***Progress in Surface Science*** **2004, 76, (3-5), 55-69.**

11. Riepl, M.; Ostblom, M.; Lundstrom, I.; Svensson, S. C. T.; van der Gon, A. W. D.; Schaferling, M.; Liedberg, B., Molecular gradients: An efficient approach for optimizing the surface properties of biomaterials and biochips. ***Langmuir*** **2005, 21, (3), 1042-1050.**

12. Rosario, R.; Gust, D.; Garcia, A. A.; Hayes, M.; Taraci, J. L.; Clement, T.; Dailey, J. W.; Picraux, S. T., Lotus effect amplifies light-induced contact angle switching. *Journal Of Physical Chemistry B* 2004, 108, (34), 12640-12642.

13. Zhu, L.; Feng, Y.; Ye, X.; Zhou, Z., Tuning wettability and getting superhydrophobic surface by controlling surface roughness with well-designed microstructures. *Sensors and Actuators, A: Physical* 2006, A130-A131, 595-600.

14. Pacifico, J.; Endo, K.; Morgan, S.; Mulvaney, P., Superhydrophobic effects of self-assembled monolayers on micropatterned surfaces: 3-D arrays mimicking the lotus leaf. *Langmuir* 2006, 22, (26), 11072-11076.

15. Yu, X.; Wang, Z. Q.; Jiang, Y. G.; Zhang, X., Surface gradient material: From superhydrophobicity to superhydrophilicity. *Langmuir* 2006, 22, (10), 4483-4486.

16. Fang, F.; Szleifer, I., Effect of molecular structure on the adsorption of protein on surfaces with grafted polymers. *Langmuir* 2002, 18, (14), 5497-5510.

17. Nath, N.; Hyun, J.; Ma, H.; Chilkoti, A., Surface engineering strategies for control of protein and cell interactions. *Surface Science* 2004, 570, (1-2), 98-110.

18. Xia, F.; Feng, L.; Wang, S. T.; Sun, T. L.; Song, W. L.; Jiang, W. H.; Jiang, L., Dual-responsive surfaces that switch superhydrophilicity and superhydrophobicity. *Advanced Materials* 2006, 18, (4), 432-+.

19. McHale, G.; Shirtcliffe, N. J.; Newton, M. I., Contact-angle hysteresis on super-hydrophobic surfaces. *Langmuir* 2004, 20, (23), 10146-10149.

20. Nakajima, A.; Hashimoto, K.; Watanabe, T., Recent Studies on Super-Hydrophobic Films. *Monatshefte fur Chemie* 2001, 132, (1), 31-41.

21. Barthlott, W.; Neinhuis, C., Purity of the sacred lotus, or escape from contamination in biological surfaces. *Planta* 1997, 202, (1), 1-8.

22. Ruardy, T. G.; Schakenraad, J. M.; van der mei, H. C.; Busscher, H. J., Preparation and characterization of chemical gradient surfaces and their application for the study of cellular interaction phenomena. *Surface Science Reports* 1997, 29, (1), 1-30.

23. Xu, C.; Wu, T.; Batteas, J. D.; Drain, C. M.; Beers, K. L.; Fasolka, M. J., Surface-grafted block copolymer gradients: Effect of block length on solvent response. *Applied Surface Science* 2006, 252, (7), 2529-2534.

24. Choi, I.; Kang, S. K.; Lee, J.; Kim, Y.; Yi, J., In situ observation of biomolecules patterned on a PEG-modified Si surface by scanning probe lithography. *Biomaterials* 2006, 27, (26), 4655-4660.

25. Collins, B. E.; Dancil, K.-P. S.; Abbi, G.; Sailor, M. J., Determining protein size using an electrochemically machined pore gradient in silicon. ***Advanced Functional Materials*** **2002, 12, (3), 187-191.**

26. Jedamzik, R.; Neubrand, A.; Rodel, J., Production of functionally graded materials from electrochemically modified carbon preforms. ***Journal Of The American Ceramic Society*** **2000, 83, (4), 983-985.**

27. Li, Y. Y.; Kim, P.; Sailor, M. J., Painting a rainbow on silicon - a simple method to generate a porous silicon band filter gradient. ***Physica Status Solidi A: Applications and Materials Science*** **2005, 202, (8), 1616-1618.**

28. Karlsson, L. M.; Schubert, M.; Ashkenov, N.; Arwin, H., Adsorption of human serum albumin in porous silicon gradients monitored by spatially-resolved spectroscopic ellipsometry. ***Phys. Status Solidi C: Conferences and Critical Reviews*** **2005, 2, 3293-3297.**

29. Bico, J.; Thiele, U.; Quere, D., Wetting of textured surfaces. ***Colloids and Surfaces a-Physicochemical and Engineering Aspects*** **2002, 206, (1-3), 41-46.**

30. Herbertson, D. L.; Evans, C. R.; Shirtcliffe, N. J.; McHale, G.; Newton, M. I., Electrowetting on superhydrophobic SU-8 patterned surfaces. ***Sensors and Actuators a-Physical*** **2006, 130, 189-193.**

31. Low, S. P.; Williams, K. A.; Canham, L. T.; Voelcker, N. H., Evaluation of mammalian cell adhesion on surface-modified porous silicon. ***Biomaterials*** **2006, 27, (26), 4538-4546.**

32. Lowe, R.; Go, E. P.; Tong, G. C.; Voelcker, N. H.; Siuzdak, G., Monitoring EDTA and endogenous metabolite biomarkers from serum with mass spectrometry. ***Spectroscopy-an International Journal*** **2005, 19, (3), 137-146.**

33. Bisi, O.; Ossicini, S.; Pavesi, L., Porous silicon: a quantum sponge structure for silicon based optoelectronics. ***Surface Science Reports*** **2000, 38, (1-3), 1-126.**

34. Ignatieva, L. N.; Tsvetnikov, A. K.; Livshits, A. N.; Saldin, V. I.; Buznik, V. M., Spectroscopic Study of Modified Polytetrafluoroethylene ***Journal of Structural Chemistry*** **2002, 43, 64-68.**

35. Nishino, T.; Meguro, M.; Nakamae, K.; Matsushita, M.; Ueda, Y., The lowest surface free energy based on -CF3 alignment. ***Langmuir*** **1999, 15, (13), 4321-4323.**

36. Lafuma, A.; Quere, D., Superhydrophobic states. ***Nature Materials*** **2003, 2, (7), 457-460.**

37. Oner, D.; McCarthy, T. J., Ultrahydrophobic surfaces. Effects of topography length scales on wettability. ***Langmuir*** **2000, 16, (20), 7777-7782.**

38. Narhe, R. D.; Beysens, D. A., Water condensation on a super-hydrophobic spike surface. ***Europhysics Letters*** **2006, 75, (1), 98-104.**

39. Li, J.; Fu, J.; Cong, Y.; Wu, Y.; Xue, L. J.; Han, Y. C., Macroporous fluoropolymeric films templated by silica colloidal assembly: A possible route to super-hydrophobic surfaces. *Applied Surface Science* 2006, 252, (6), 2229-2234.

40. Chen, W.; Fadeev, A. Y.; Hsieh, M. C.; Oner, D.; Youngblood, J.; McCarthy, T. J., Ultrahydrophobic and ultralyophobic surfaces: Some comments and examples. *Langmuir* 1999, 15, (10), 3395-3399.

41. Zhao, J. Y.; Li, Y. H.; Guo, H. Q.; Gao, L. X., Relative surface density and stability of the amines on the bio-chip. *Chinese Journal of Analytical Chemistry* 2006, 34, (9), 1235-1238.

42. Cebeci, F. C.; Wu, Z. Z.; Zhai, L.; Cohen, R. E.; Rubner, M. F., Nanoporosity-driven superhydrophilicity: A means to create multifunctional antifogging coatings. *Langmuir* 2006, 22, (6), 2856-2862.

43. McHale, G.; Shirtcliffe, N. J.; Aqil, S.; Perry, C. C.; Newton, M. I., Topography driven spreading. *Physical Review Letters* 2004, 93, (3).

44. Shirtcliffe, N. J.; McHale, G.; Newton, M. I.; Perry, C. C.; Roach, P., Porous materials show superhydrophobic to superhydrophilic switching. *Chemical Communications* 2005, (25), 3135-3137.

45. Quere, D.; Lafuma, A.; Bico, J., Slippy and sticky microtextured solids. *Nanotechnology* 2003, 14, (10), 1109-1112.

46. Spradling, A.; Drummond-Barbosa, D.; Kai, T., Stem cells find their niche. *Nature (London, United Kingdom)* 2001, 414, (6859), 98-104.

47. Streuli, C., Extracellular matrix remodelling and cellular differentiation. *Current Opinion in Cell Biology* 1999, 11, (5), 634-640.

48. Glass-Brudzinski, J.; Perizzolo, D.; Brunette, D. M., Effects of substratum surface topography on the organisation of cells and collagen fibers in collagen gel cultures. *Journal of Biomedical Materials Research* 2002, 61, (4), 608-618.

49. Teixeira, A. I.; Nealey, P. F.; Murphy, C. J., Responses of human keratocytes to micro- and nanostructured substrates. *Journal of Biomedical Materials Research, Part A* 2004, 71A, (3), 369-376.

50. Backman, L., Shape changes of the human red cell studied by aqueous two-phase partition. *FEBS Letters* 1990, 262, (1), 107-10.

51. Salloum, D. S.; Olenych, S. G.; Keller, T. C. S.; Schlenoff, J. B., Vascular smooth muscle cells on polyelectrolyte multilayers: hydrophobicity-directed adhesion and growth. *Biomacromolecules* 2005, 6, (1), 161-167.

52. Zelezetsky, I.; Pacor, S.; Pag, U.; Papo, N.; Shai, Y.; Sahl, H.-G.; Tossi, A., Controlled alteration of the shape and conformational stability of a-helical cell-lytic

peptides: effect on mode of action and cell specificity. *Biochemical Journal* 2005, 390, (1), 177-188.

53. Cyster, L. A.; Parker, K. G.; Parker, T. L.; Grant, D. M., The effect of surface chemistry and nanotopography of titanium nitride (TiN) films on 3T3-L1 fibroblasts. *Journal of Biomedical Materials Research, Part A* 2003, 67A, (1), 138-147.

54. Kapur, R.; Rudolph, A. S., Cellular and cytoskeleton morphology and strength of adhesion of cells on self-assembled monolayers of organosilanes. *Experimental Cell Research* 1998, 244, (1), 275-285.

55. Suh, J.-Y.; Jang, B.-C.; Zhu, X.; Ong, J. L.; Kim, K., Effect of hydrothermally treated anodic oxide films on osteoblast attachment and proliferation. *Biomaterials* 2002, 24, (2), 347-355.

56. Becker, J. W.; Erickson, H. P.; Hoffman, S.; Cunningham, B. A.; Edelman, G. M., Topology of cell adhesion molecules [Erratum to document cited in CA110(21):187977d]. *Proceedings of the National Academy of Sciences of the United States of America* 1989, 86, (14), 5670.

57. Sherratt, M. J.; Bax, D. V.; Chaudhry, S. S.; Hodson, N.; Lu, J. R.; Saravanapavan, P.; Kielty, C. M., Substrate chemistry influences the morphology and biological function of adsorbed extracellular matrix assemblies. *Biomaterials* 2005, 26, (34), 7192-7206.

58. Timpl, R., Macromolecular organisation of basement membranes. *Current Opinion in Cell Biology* 1996, 8, (5), 618-624.

59. Harrison, R. G., The cultivation of tissues in extraneous media as a method of morphogenetic study. *Anat Rec* 1912, 6, (181-193).

60. Weiss, P., In Vitro Experiments on the Factors Determining the course of the outgrowing nerve fiber. *The Journal of Experimental zoology* 1934, 68, (3), 393-448.

61. Weiss, P., Experiments on cell and axon orientation in vitro: The role of colloidal exdudates in tissue organisation. *Journal of Experimental Zoology* 1945, 100, 353-386.

62. Bettinger, C. J.; Orrick, B.; Misra, A.; Langer, R.; Borenstein, J. T., Microfabrication of poly(glycerol-sebacate) for contact guidance applications. *Biomaterials* 2006, 27, (12), 2558-2565.

63. Charest, J. L.; Bryant, L. E.; Garcia, A. J.; King, W. P., Hot embossing for micropatterned cell substrates. *Biomaterials* 2004, 25, (19), 4767-4775.

64. Schindler, M.; Ahmed, I.; Kamal, J.; Nur-E-Kamal, A.; Grafe, T. H.; Young Chung, H.; Meiners, S., A synthetic nanofibrillar matrix promotes in vivo-like organisation and morphogenesis for cells in culture. *Biomaterials* 2005, 26, (28), 5624-5631.

65. Tan, J.; Saltzman, W. M., Topographical control of human neutrophil motility on micropatterned materials with various surface chemistry. *Biomaterials* 2002, 23, (15), 3215-3225.

66. Karlsson, L. M.; Schubert, M.; Ashkenov, N.; Arwin, H., Protein adsorption in porous silicon gradients monitored by spatially-resolved spectroscopic ellipsometry. *Thin Solid Films* 2004, 455-56, 726-730.

67. Bayliss, S. C.; Buckberry, L. D.; Fletcher, I.; Tobin, M. J., The culture of neurons on silicon. *Sensors and Actuators, A: Physical* 1999, A74, (1-3), 139-142.

68. Bayliss, S. C.; Buckberry, L. D.; Harris, P. J.; Tobin, M., Nature of the silicon-animal cell interface. *Journal of Porous Materials* 2000, 7, (1/2/3), 191-195.

69. Bayliss, S. C.; Heald, R.; Fletcher, D. I.; Buckberry, L. D., The culture of mammalian cells on nanostructured silicon. *Advanced Materials (Weinheim, Germany)* 1999, 11, (4), 318-321.

70. Chin, V.; Collins, B. E.; Sailor, M. J.; Bhatia, S. N., Compatibility of primary hepatocytes with oxidized nanoporous silicon. *Advanced Materials* 2001, 13, (24), 1877-+.

71. Johansson, F.; Carlberg, P.; Danielsen, N.; Montelius, L.; Kanje, M., Axonal outgrowth on nano-imprinted patterns. *Biomaterials* 2006, 27, (8), 1251-1258.

72. Zhang, J. Y.; Venkataramani, S.; Xu, H.; Song, Y. K.; Song, H. K.; Palmore, G. T. R.; Fallon, J.; Nurmikko, A. V., Combined topographical and chemical micropatterns for templating neuronal networks. *Biomaterials* 2006, 27, (33), 5734-5739.

73. Matsuzawa, M.; Krauthamer, V.; Potember, R. S., Directional guidance of neurite outgrowth using substrates patterned with biomaterials. *Biosystems* 1995, 35, (2-3), 199-202.

74. Matsuzawa, M.; Potember, R. S.; Stenger, D. A.; Krauthamer, V., Containment and growth of neuroblastoma cells on chemically patterned substrates. *Journal of neuroscience methods* 1993, 50, (2), 253-60.

75. Cos, S.; Verduga, R.; Fernandez-Viadero, C.; Megias, M.; Crespo, D., Effects of melatonin on the proliferation and differentiation of human neuroblastoma cells in culture. *Neuroscience Letters* 1996, 216, (2), 113-116.

76. Zagon, I. S.; McLaughlin, P. J., Opioids and differentiation in human cancer cells. *Neuropeptides (Amsterdam, Netherlands)* 2005, 39, (5), 495-505.

77. Ben, L.-H.; Zhao, J.; Xin, S.-M.; Luo, S.-Q.; Pei, G., Attenuation of d opioid receptor-mediated signaling by kainic acid in neural cells: involvement of protein kinase C and intracellular Ca2+. *Neuropharmacology* 1999, 38, (7), 991-998.

78. Los, G. V.; Artemenko, I. P.; Hokin, L. E., Time-dependent effects of lithium on the agonist-stimulated accumulation of second messenger inositol 1,4,5-trisphosphate in SH-SY5Y human neuroblastoma cells. *Biochemical Journal* 1995, 311, (1), 225-32.

79. Moolwaney, A. S.; Igwe, O. J., Regulation of the cyclooxygenase-2 system by interleukin-1b through mitogen-activated protein kinase signaling pathways: A comparative study of human neuroglioma and neuroblastoma cells. *Molecular Brain Research* 2005, 137, (1-2), 202-212.

80. Glicklis, R.; Shapiro, L.; Agbaria, R.; Merchuk, J. C.; Cohen, S., Hepatocyte behavior within three-dimensional porous alginate scaffolds. *Biotechnology and Bioengineering* 2000, 67, (3), 344-353.

81. Matsuzaka, K.; Walboomers, F.; de Ruijter, A.; Jansen, J. A., Effect of microgrooved poly-l-lactic (PLA) surfaces on proliferation, cytoskeletal, organisation and mineralized matrix formation of rat bone marrow cells. *Clinical oral implants research* 2000, 11, (4), 325-33.

82. Cooper, M. W.; Smith, S. J. A real-time analysis of growth cone-target cell interactions during the formation of stable contacts between hippocampal neurons in culture., *Journal of Neurobiology* 1992, 23, (7), 814-828.

83. Koleske Anthony, J., Do Filopodia Enable the Growth Cone to Find Its Way? *Sci. STKE* 2003, 2003, (183), pe20.

84. Annaz, B.; Hing, K. A.; Kayser, M.; Buckland, T.; Di Silvio, L., Porosity variation in hydroxyapatite and osteoblast morphology: a scanning electron microscopy study. *Journal of Microscopy-Oxford* 2004, 215, 100-110.

85. Tirrell, M.; Kokkoli, E.; Biesalski, M., The role of surface science in bioengineered materials. *Surface Science* 2002, 500, (1-3), 61-83.

86. Yim, E. K. F.; Leong, K. W., Significance of synthetic nanostructures in dictating cellular response. *Nanomedicine* 2005, 1, (1), 10-21.

87. Zhao, G.; Schwartz, Z.; Wieland, M.; Rupp, F.; Geis-Gerstorfer, J.; Cochran, D. L.; Boyan, B. D., High surface energy enhances cell response to titanium substrate microstructure. *Journal of Biomedical Materials Research, Part A* 2005, 74A, (1), 49-58.

88. Barnes, E. N.; Biedler, J. L.; Spengler, B. A.; Lyser, K. M., The fine structure of continuous human neuroblastoma lines SK-N-SH, SK-N-BE(2), and SK-N-MC. *In vitro* 1981, 17, (7), 619-31.

89. Schlesinger, H. R.; Gerson, J. M.; Moorhead, P. S.; Maguire, H.; Hummeler, K., Establishment and characterization of human neuroblastoma cell lines. *Cancer Research* 1976, 36, (9, Pt. 1), 3094-100.

90. Seeger, R. C.; Rayner, S. A.; Banerjee, A.; Chung, H.; Laug, W. E.; Neustein, H. B.; Benedict, W. F., Morphology, growth, chromosomal pattern and fibrinolytic activity of two new human neuroblastoma cell lines. *Cancer research* 1977, 37, (5), 1364-71.

91. Rovensky, Y. A.; Samoilov, V. I., Morphogenetic response of cultured normal and transformed fibroblasts, and epitheliocytes, to a cylindrical substratum surface.

Possible role for the actin filament bundle pattern . *Journal of Cell Science* 1994, 107, 1255-1263.

92. Mitchison, T. J.; Cramer, L. P., Actin-based cell motility and cell locomotion. *Cell* 1996, 84, (3), 371-379.

93. Clark, P.; Connolly, P.; Moores, G. R., Cell guidance by micropatterned adhesiveness invitro. *Journal of Cell Science* 1992, 103, 287-292.

94. Hamilton, D. W.; Brunette, D. M., "Gap guidance" of fibroblasts and epithelial cells by discontinuous edged surfaces. *Experimental Cell Research* 2005, 309, (2), 429-437.

95. Fan, S.; Ramirez, S. H.; Garcia, T. M.; Dewhurst, S., Dishevelled promotes neurite outgrowth in neuronal differentiating neuroblastoma 2A cells, via a DIX-domain dependent pathway. *Molecular Brain Research* 2004, 132, (1), 38-50.

96. Miloso, M.; Villa, D.; Crimi, M.; Galbiati, S.; Donzelli, E.; Nicolini, G.; Tredici, G., Retinoic acid-induced neuritogenesis of human neuroblastoma SH-SY5Y cells is ERK independent and PKC dependent. *Journal of Neuroscience Research* 2003, 75, (2), 241-252.

97. Simpson, P. B.; Bacha, J. I.; Palfreyman, E. L.; Woollacott, A. J.; McKernan, R. M.; Kerby, J., Retinoic acid-evoked differentiation of neuroblastoma cells predominates over growth factor stimulation: an automated image capture and quantitation approach to neuritogenesis. *Analytical Biochemistry* 2001, 298, (2), 163-169.

98. Thomas, J. J.; Shen, Z.; Crowell, J. E.; Finn, M. G.; Siuzdak, G., Desorption/ionization on silicon (DIOS): a diverse mass spectrometry platform for protein characterization. *Proceedings of the National Academy of Sciences of the United States of America* 2001, 98, (9), 4932-4937.

99. Khung, Y. L.; Graney, S. D.; Voelcker, N. H., Micropatterning of porous silicon films by direct laser writing. *Biotechnology Progress* 2006, 22, (5), 1388-1393.

100. Arsenault, A.; Fournier-Bidoz, S. B.; Hatton, B.; Miguez, H.; Tetrault, N.; Vekris, E.; Wong, S.; Yang, S. M.; Kitaev, V.; Ozin, G. A., Towards the synthetic all-optical computer: science fiction or reality? *Journal of Materials Chemistry* 2004, 14, (5), 781-794.

101. Greene, K., World's fastest optical chip. *Technology Review* 2007, 110, (1), 78-80.

102. Wa, P. L. K., Intermixing of Multiple Quantum-Wells for All-Optical Integrated-Circuits. *Optical and Quantum Electronics* 1991, 23, (7), S925-S939.

103. Weiss, S. M.; Haurylau, M.; Fauchet, P. M., Tunable photonic bandgap structures for optical interconnects. *Optical Materials* 2005, 27, (5), 740-744.

104. Bruyant, A.; Lerondel, G.; Reece, P. J.; Gal, M., All-silicon omnidirectional mirrors based on one-dimensional photonic crystals. *Applied Physics Letters* 2003, 82, (19), 3227-3229.

105. Huang, C. K.; Chan, C. H.; Chen, C. Y.; Tsai, Y. L.; Chen, C. C.; Han, J. L.; Hsieh, K. H., Rapid fabrication of 2D and 3D photonic crystals and their inversed structures. *Nanotechnology* 2007, 18, (26).

106. Marsh, J. H.; Bryce, A. C.; DeLaRue, R. M.; McLean, C. J.; McKee, A.; Lullo, G., Fabrication of quantum well photonic integrated circuits using laser processing. *Applied Surface Science* 1996, 106, 326-334.

107. Agarwal, V.; del Rio, J. A., Tailoring the photonic band gap of a porous silicon dielectric mirror. *Applied Physics Letters* 2003, 82, (10), 1512-1514.

108. Anglin, E. J.; Schwartz, M. P.; Ng, V. P.; Perelman, L. A.; Sailor, M. J., Engineering the chemistry and nanostructure of porous Silicon Fabry-Perot films for loading and release of a steroid. *Langmuir* 2004, 20, (25), 11264-11269.

109. Canham, L. T.; Stewart, M. P.; Buriak, J. M.; Reeves, C. L.; Anderson, M.; Squire, E. K.; Allcock, P.; Snow, P. A., Derivatized porous silicon mirrors: Implantable optical components with slow resorbability. *Physica Status Solidi a-Applied Research* 2000, 182, (1), 521-525.

110. Guillermain, E.; Lysenko, V.; Benyattou, T., Surface wave photonic device based on porous silicon multilayers. *Journal of Luminescence* 2006, 121, (2), 319-321.

111. Ilyas, S.; Bocking, T.; Kilian, K.; Reece, P. J.; Gooding, J.; Gaus, K.; Gal, M., Porous silicon based narrow line-width rugate filters. *Optical Materials* 2007, 29, (6), 619-622.

112. Kavokin, A. V.; Malpuech, G.; Shelykh, I., Negative refraction of light in Bragg mirrors made of porous silicon. *Physics Letters A* 2005, 339, (3-5), 387-392.

113. Lee, B. J.; Kim, S. G.; Sohn, H., Optically encoded smart dust from DBR porous silicon. In *Advanced Nondestructive Evaluation I, Pts 1 and 2, Proceedings*, 2006; Vol. 321-323, pp 53-56.

114. Lorenzo, E.; Oton, C. J.; Capuj, N. E.; Ghulinyan, M.; Navarro-Urrios, D.; Gaburro, Z.; Pavesi, L., Porous silicon-based rugate filters. *Applied Optics* 2005, 44, (26), 5415-5421.

115. Ohno, Y.; Ozaki, N.; Takeda, S., Fabrication of periodic nanohole multilayer structure on silicon surface toward photonic crystal. *Physica B-Condensed Matter* 2001, 308, 1222-1225.

116. Perez, E. X.; Marsal, L. F.; Ferre-Borrull, J.; Trifonov, T.; Pallares, J., Influence of the humidity conditions on the reflectivity spectrum of a porous silicon microcavity. *Physica E-Low-Dimensional Systems & Nanostructures* 2007, 38, (1-2), 172-175.

117. Qian, M.; Bao, X. Q.; Wang, L. W.; Lu, X.; Shao, J.; Chen, X. S., Structural tailoring of multilayer porous silicon for photonic crystal application. ***Journal of Crystal Growth*** **2006, 292, (2), 347-350.**

118. Rendina, I.; Rea, I.; Rotiroti, L.; De Stefano, L., Porous silicon-based optical biosensors and biochips. ***Physica E-Low-Dimensional Systems & Nanostructures*** **2007, 38, (1-2), 188-192.**

119. Salem, M. S.; Sailor, M. J.; Sakka, T.; Ogata, Y. H., Electrochemical preparation of a rugate filter in silicon and its deviation from the ideal structure. ***Journal of Applied Physics*** **2007, 101, (6).**

120. Vincent, G., Optical-Properties Of Porous Silicon Superlattices. ***Applied Physics Letters*** **1994, 64, (18), 2367-2369.**

121. Janshoff, A.; Dancil, K. P. S.; Steinem, C.; Greiner, D. P.; Lin, V. S. Y.; Gurtner, C.; Motesharei, K.; Sailor, M. J.; Ghadiri, M. R., Macroporous p-type silicon Fabry-Perot layers. Fabrication, characterization, and applications in biosensing. ***Journal Of The American Chemical Society*** **1998, 120, (46), 12108-12116.**

122. Cullis, A. G.; Canham, L. T.; Calcott, P. D. J., The structural and luminescence properties of porous silicon. ***Journal of Applied Physics*** **1997, 82, (3), 909-965.**

123. Stewart, M. P.; Buriak, J. M., Chemical and biological applications of porous silicon technology. ***Advanced Materials*** **2000, 12, (12), 859-869.**

124. Arroyo-Hernandez, M.; Martin-Palma, R. J.; Torres-Costa, V.; Martinez Duart, J. M., Porous silicon optical filters for biosensing applications. ***Journal of Non-Crystalline Solids*** **2006, 352, (23-25), 2457-2460.**

125. Mangaiyarkarasi, D.; Breese, M. B. H.; Sheng, O. Y.; Ansari, K.; Vijila, C.; Blackwood, D., Porous silicon-based Bragg reflectors and Fabry-Perot interference filters for photonic applications. ***Proceedings of SPIE-The International Society for Optical Engineering*** **2006, 6125, (Silicon Photonics), 61250X/1-61250X/8.**

126. Mazzoleni, C.; Pavesi, L., Application to optical components of dielectric porous silicon multilayers. ***Applied Physics Letters*** **1995, 67, (20), 2983-5.**

127. Pavesi, L.; Dubos, P., Random porous silicon multilayers: application to distributed Bragg reflectors and interferential Fabry-Perot filters. ***Semiconductor Science and Technology*** **1997, 12, (5), 570-575.**

128. Chapron, J.; Alekseev, S. A.; Lysenko, V.; Zaitsev, V. N.; Barbier, D., Analysis of interaction between chemical agents and porous Si nanostructures using optical sensing properties of infra-red Rugate filters. ***Sensors and Actuators B-Chemical*** **2007, 120, (2), 706-711.**

129. Kaminska, K.; Suzuki, M.; Kimura, K.; Taga, Y.; Robbie, K., Simulating structure and optical response of vacuum evaporated porous rugate filters. ***Journal of Applied Physics*** **2004, 95, (6), 3055-3062.**

130. Hunkel, D.; Butz, R.; Ares-Fisher, R.; Marso, M.; Luth, H., Interference filters from porous silicon with laterally varying wavelength of reflection. *Journal Of Luminescence* 1998, 80, (1-4), 133-136.

131. Kennedy, S. R.; Brett, M. J., Porous broadband antireflection coating by glancing angle deposition. *Applied Optics* 2003, 42, (22), 4573-4579.

132. Striemer, C. C.; Fauchet, P. M., Dynamic etching of silicon for solar cell applications. *Physica Status Solidi A-Applied Research* 2003, 197, (2), 502-506.

133. Bohn, H. G.; Marso, M., Wedge-shaped layers from porous silicon: the basics of laterally graded interference filters. *Physica Status Solidi a-Applications and Materials Science* 2005, 202, (8), 1437-1442.

134. Ouyang, H.; Fauchet, P. M., Biosensing using Porous Silicon Photonic Bandgap Structures. *SPIE Optics East* 2005, 6005, 600508-1.

135. Foss, S. E.; Finstad, T. G., Laterally Graded Rugate Filters in Porous Silicon. *Material Research Society Symposium Proceedings* 2004, 797, W1.6.1-W1.6.6.

136. Cunin, F.; Milhiet, P. E.; Anglin, E.; Sailor, M. J.; Espenel, C.; Le Grimellec, C.; Brunel, D.; Devoisselle, J. M., Continuous planar phospholipid bilayer supported on porous silicon thin film reflector. *Ultramicroscopy* 2007, 107, (10-11), 1048-1052.

137. Hunkel, D.; Marso, M.; Butz, R.; Arens-Fischer, R.; Luth, H., Integrated photometer with porous silicon interference filters. *Materials Science and Engineering B-Solid State Materials for Advanced Technology* 2000, 69, 100-103.

138. Meade, S. O.; Yoon, M. S.; Ahn, K. H.; Sailor, M. J., Porous silicon photonic crystals as encoded microcarriers. *Advanced Materials* 2004, 16, (20), 1811-+.

139. Xie, R. G.; Li, D. S.; Zhang, H.; Yang, D. R.; Jiang, M. H.; Sekiguchi, T.; Liu, B. D.; Bando, Y., Low-temperature growth of uniform ZnO particles with controllable ellipsoidal morphologies and characteristic luminescence patterns. *Journal Of Physical Chemistry B* 2006, 110, (39), 19147-19153.